J Mater Sci: Mater Electron **(2025) 36:2088**

Synthesis and various DFT calculations of new Cd(II) crystal as dual-tasking complex in NLO and α-glucosidase inhibitory activities

Davut Avcı[1,*], Fatih Sönmez[2], Adil Başoğlu[1], Ömer Tamer[1], Yusuf Atalay[1], Necmi Dege[3], and Belma Zengin Kurt[4]

[1] *Faculty of Science, Department of Physics, Sakarya University, 54187 Sakarya, Turkey*
[2] *Sakarya University of Applied Sciences, Pamukova Vocational High School, 54055 Sakarya, Turkey*
[3] *Faculty of Science, Department of Physics, Ondokuz Mayıs University, 55139 Samsun, Turkey*
[4] *Faculty of Pharmacy, Department of Pharmaceutical Chemistry, Bezmialem Vakif University, 34093 Istanbul, Turkey*

Received: 10 September 2025
Accepted: 29 October 2025
Published online: 17 November 2025

ABSTRACT

The structure of the newly synthesized Cd(II) complex of 6-chloropyridine-2-carboxylic acid (6-ClPCA) was determined by the XRD method. The molecular structure was confirmed via single-crystal X-ray diffraction, while vibrational and electronic properties were investigated through FT-IR, UV–Vis spectroscopy, and DFT-based quantum chemical calculations. Five different DFT functionals were employed to optimize the molecular geometry and predict vibrational spectra, with statistical fitting parameters (MAD, RMS, MPD%, R^2) applied to evaluate consistency with experimental data. The nonlinear optical (NLO) behavior of the complex was assessed using the Z–scan technique, revealing promising second-order hyperpolarizability values. In addition, enzyme inhibition assays and molecular docking studies were conducted to explore the biological potential of the Cd(II) complex, with notable binding affinities observed toward target enzymes. This integrated approach addresses several gaps in the literature by combining structural elucidation, electronic property analysis, NLO performance, and bioactivity evaluation within a single framework. Furthermore, the linear optical (LO), $\chi^{(1)}/P^{(1)}$, second−, and third−order NLO, $\chi^{(2)}/P^{(2)}$ and $\chi^{(3)}/P^{(3)}$, susceptibility tensors/polarization parameters for Cd(II) complex were obtained at DFT/CAM-B3LYP and DFT/HSEh1PBE levels. At the same DFT levels, the *E*, *P*, and *D* (external electric field, polarization, and electric displacement, respectively) values of the Cd(II) complex were also computed. In addition, the refractive index (*n*) and optical band gap were determined in the UV–Vis region. DFT/CAM-B3LYP and DFT/HSEh1PBE levels were applied to investigate static and frequency–dependent LO and NLO parameters for the Cd(II) complex. The *E*, *P*, and *D* parameters for Cd(II) complex were found to be $1.614/4.314 \times 10^9$ V/m, $4.042/6.525 \times 10^{-2}$ C/m^2, and $5.471/2.705 \times 10^{-2}$ C/m^2, respectively. These results

Address correspondence to E-mail: davci@sakarya.edu.tr

https://doi.org/10.1007/s10854-025-16136-5

indicate that the Cd(II) complex has a strong electronic response. Based on the Z–scan results, third−order NLO susceptibility ($\chi^{(3)}$) and second−order molecular hyperpolarizability (γ) for the complex were obtained at 1876.62×10^{-4} and -4676.33×10^{-28} esu, respectively. Moreover, using DFT/CAM-B3LYP level, the $<\gamma(0;0,0,0)>$ / $<\gamma(-\omega;\omega,0,0)>$ and $<\gamma(-2\omega;\omega,\omega,0)>$ in ethanol were calculated at 3407.19×10^{-36}, − 1,974,417.9 × 10^{-36}, and − 15182.76 × 10^{-36} esu, respectively. The IC_{50} value of the Cd(II) complex for α-glucosidase inhibition was determined at 383.71 ± 1.54 μM. While a low level of measurable result was obtained against α-glucosidase for the Cd(II) complex, the NLO parameter determined in the third order with the Z–scan technique, and the second− and third−order calculated NLO results showed the potential of being a suitable material for NLO optical devices containing environmentally responsive phase-modulating sensors and intensity-dependent detectors, etc. The findings suggest that the title complex holds potential for both optoelectronic and biomedical applications.

1 Introduction

Transition metal complexes are of great interest as optoelectronic materials and biologically active compounds. The attractiveness of these complexes stems from the fact that the optical and electronic properties resulting from the d-electron configuration of the metal ions and their interaction with the ligands can be easily modulated. In particular, pyridine-based derivatives in transition metal complexes offer a wide range of applications due to their strong coordination abilities and diverse functional groups. In this context, metal complexes containing 6-chloropyridine-2-carboxylic acid (6-ClPCA) attract attention in terms of both structural and electronic properties [1, 2].

In recent years, heterocyclic ligands such as 6-ClPCA have been able to coordinate metal ions via *N* and *O* atoms, allowing extensive studies on the complexes formed by 6-ClPCA with transition metal ions, including Zn(II), Co(II), Mn(II), and Cu(II) [1, 3, 4]. These studies indicate that such complexes hold great potential in terms of both their nonlinear optical (NLO) properties and biological activities. Moreover, picolinic acid derivatives and metal complexes are suitable for photonic, optical, and electronic applications. Metal-ligand charge transfer bands can significantly increase the nonlinear optical coefficients of these complexes [2, 3, 5]. Regarding biological activity, molecular docking analyses on Zn(II) and Cu(II) complexes of 6-ClPCA revealed that these compounds exhibited potential inhibitory properties on the SARS-CoV-2 main protease and α−glucosidase inhibitory activity [1, 3]. In brief, the attention towards these compounds stems not only from their biological activities but also from their different physicochemical and optical properties.

Recent advancements in green nanotechnology have underscored the significant role of nanostructured materials in addressing environmental challenges, catalysis, renewable energy production, and energy storage [6–17]. Among these, metal-organic complexes have garnered attention due to their tunable electronic structures and versatile coordination environments. For instance, a study by Anand et al. (2024) demonstrated the potential of Cd(II)-based coordination polymers in energy storage applications, highlighting their pseudocapacitive behavior and cost-effective synthesis [18]. Additionally, Cd(II) complexes have shown promise in electrochemical sensing, with nanocomposite materials exhibiting enhanced sensitivity and selectivity for detecting heavy metal ions [19]. These properties enable precise modulation of their optical, electrochemical, and catalytic behaviors, making Cd(II) complexes promising candidates for a wide range of sustainable technological applications.

α-Glucosidase (EC 3.2.1.20) is an important enzyme that facilitates the breakdown of carbohydrates into simple sugars through hydrolysis. Inhibition of this enzyme has become a critical strategy for controlling blood sugar, particularly in the treatment of type 2

diabetes mellitus (T2DM) [20, 21]. α-Glucosidase inhibitors (AGIs) have been shown to play a crucial role in preventing postprandial blood glucose increases by slowing down the digestive process and delaying carbohydrate absorption [20, 22]. Although AGIs such as acarbose, miglitol, and voglibose are widely used in the clinic, more effective and safer alternatives are needed due to their side effects [20, 23]. In recent decades, studies on the potential roles of metal complexes in α-glucosidase inhibition have increased [20–26]. Many studies have focused on the insulinomimetic activities of transition metals such as zinc, copper, and cadmium and their effects on enzyme inhibition [3, 20, 21, 23, 27–29]. It has been observed that biologically active complexes of these metals exhibit strong inhibitory effects on α-glucosidase, making them promising candidates for treating type 2 diabetes. Molecular docking and computational investigations are also conducted to understand the impact of metal complexes on α-glucosidase and to investigate the mechanisms of these complexes [3, 20, 21, 23, 30]. In this context, studies on the effects of transition metal complexes on α-glucosidase inhibition appear to constitute an important research area for developing new anti-diabetes agents using organic small molecules and metal complexes [1, 3, 20]. Such studies reveal that Cd(II) complexes are promising both structurally and in terms of biological activity. In short, the use of Cd(II) and similar metal complexes in treating type 2 diabetes indicates that this area is ripe for further research and development in the coming years.

Density Functional Theory (DFT) plays a crucial role in elucidating the electronic structures and molecular characteristics, particularly in transition metal complexes. The ability of DFT to predict the electronic structures of systems makes it widely used in both experimental and theoretical studies [31, 32]. DFT is one of the most common methods used to study the structural, electronic, and optical properties of metal complexes. However, its accuracy depends mainly on the choice of the function used [5, 33, 34]. The effectiveness of DFT in electronic structure calculations varies depending on the choice of functional. Various DFT methods, including GGA, meta-GGA, hybrid GGA, and long-range decoupled hybrid functionals, each offer distinct advantages and disadvantages [5, 35]. For example, meta-GGA functionals (e.g., M06-L, M06-2X) offer speed and cost advantages in accurately calculating molecular properties. In contrast, hybrid functionals (e.g., B3LYP, B3PW91) effectively reduce electronic density localization errors by adding Hartree-Fock exchange. DFT is also used to explore and assess the interplay between the structural and optical features of transition metal complexes. Accurate calculation of metal-ligand bond energies is one of the challenges of DFT, and hybrid functionals often give better results in this regard [34, 35]. Since NLO (Non-Linear Optics) properties are related to factors such as metal ions and coordination environments, especially in systems like metal complexes, DFT is used as an essential tool in predicting the NLO responses of such complexes. Functionals such as M06-L, B3LYP, and CAM-B3LYP are frequently preferred methods for calculating NLO properties, and their effects on different systems are comparatively studied [5, 33].

This research seeks to explore the nonlinear optical and anti-diabetic properties of the Cd(II) transition metal complex of 6-chloropyridine-2-carboxylic acid. The electronic structures and nonlinear optical responses of the first synthesized Cd(II) complex as a crystal structure were discussed in detail through spectral analysis and DFT calculations and the α-glucosidase activity was investigated. Structural and vibrational spectral parameters were computed using five distinct DFT functionals (B3PW91, B3LYP, CAM-B3LYP, ωB97XD, and HSEh1PBE) to assess their consistency with experimental observations. To determine the most accurate method, vibrational frequencies were further evaluated through statistical parameters such as MAD, RMS, MPD%, and R^2. Additionally, Z–scan measurements were carried out to determine the complex's NLO properties, and enzyme inhibition assays were supported by molecular docking simulations to examine its biological activity. To summarize, the structure-activity relationships (SAR) of this complex were first explored through a molecular docking study, which analyzed complex-protein interactions and reviewed *in vitro* findings. In addition, the Z–scan method for assessing third-order NLO characteristics, along with additional features, is discussed in detail through DFT approaches. By addressing multiple gaps in current research, including the lack of fully characterized NLO-active complexes with confirmed biological relevance, this study offers a multidisciplinary contribution that bridges theoretical chemistry, spectroscopy, photonics, and bioactivity profiling. The results position this novel complex as a promising candidate for future applications in both optoelectronic

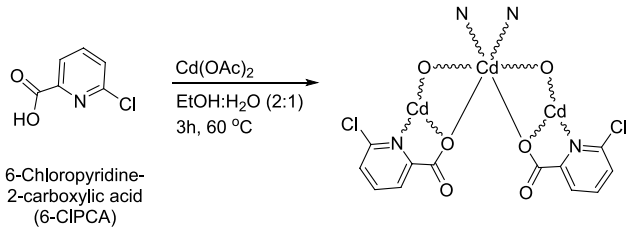

Scheme 1 The synthesis of the Cd(II) complex

device development and the discovery of therapeutic agents.

2 Experimental and computational details

2.1 The synthesis and physical tools of the Cd(II) complex {[Cd(6-ClPCA)$_2$]$_n$}

All chemicals used are commercially available analytical-grade products. 6-Chloropyridine-2-carboxylic acid (6-ClPCA) and cadmium(II) acetate ($Cd(OAc)_2$) were obtained from Sigma-Aldrich and utilized as received.

The structural and spectral properties of the Cd(II) complex were studied using the X-ray diffraction (XRD) method [36–38], and the details are given in the supplementary material. The FT-IR spectra of 6-ClPCA and the Cd(II) complex were recorded using a Perkin Elmer Spectrum-Two FT-IR spectrophotometer equipped with a Perkin Elmer UATR-TWO diamond ATR accessory. UV-Vis electronic absorption spectra of the Cd(II) complex were measured in ethanol using a HITACHI U-2900 spectrophotometer with a 1 cm quartz cuvette over the wavelength range of 200–600 nm.

The third-order nonlinear optical parameters of the Cd(II) complex, namely the nonlinear refractive index (n_2) and the nonlinear absorption coefficient (β), were determined using Z–scan measurements on a 1 mm thick sample. A continuous-wave Argon-ion laser operating at 514 nm with an output power of 28.19 mW served as the excitation source. The corresponding laser intensity at the focal point was calculated to be $I_0 = 272.11\ kW \cdot m^{-2}$.

As indicated by Scheme 1, the Cd(II) complex was synthesized by dissolving 0.5 mmol (0.115 g) of cadmium(II) acetate in 15 mL of an ethanol/water mixture (2:1) and subsequently adding 1 mmol (0.157 g) of 6-ClPCA. The mixture was stirred in a sealed vial at 60 °C for 3 h, then allowed to evaporate at room temperature. The colorless, rod-shaped single crystals were obtained in 57% yield (0.242 g) after 7 days.

2.2 The evaluation of α-glucosidase inhibitory activity

The inhibitory effect of the Cd(II) complex on α-glucosidase was determined using an altered version of Sun's procedure [21–26, 39]. In this assay, p-nitrophenyl-α-D-glucopyranoside (pNGP, Sigma, N1377) was used as the substrate, and α-glucosidase from Saccharomyces *cerevisiae* (Sigma, G5003) served as the target enzyme. The Cd(II) complex and genistein solutions were prepared in DMSO, while enzyme and substrate solutions were formulated in a 0.05 M potassium phosphate buffer (pH 6.8). The reaction solution, consisting of 20 µL α-glucosidase (0.02 U), 30 µL substrate (1.25 mM), 10 µL complex, and 140 µL buffer, was incubated at 37 °C for 30 min. Following incubation, the absorbance of the yellow-colored p-nitrophenol formed was measured at 405 nm using a Synergy H1 (BioTek, USA) 96-well microplate reader. All measurements were conducted in triplicate, and the inhibitory activity of the Cd complex against α-glucosidase was calculated using the $I\% = [(A_c\text{-}A_s)/A_c] \times 100$ equation. In this equation, A_s represents the sample's absorbance and A_c that of the control, with the IC_{50} calculated using the GraphPad Software.

2.3 Computational details

All computations to elucidate the structural, spectral, and nonlinear optical features of the synthesized Cd(II) complex were carried out using Gaussian 16, Revision C.01 [40] and GaussView 6 [41]. Initially, the structural parameters and vibrational wavenumbers of the Cd(II) complex were determined by using density functional theory (DFT) methods including B3PW91, B3LYP, CAM-B3LYP, ωB97XD, and HSEh1PBE [42–47] with the LanL2DZ [48] basis set. After these calculations, the experimental bond lengths and angles data corresponding to the theoretical results obtained using these methods were evaluated in terms of the parameters of linear correlation coefficients (R^2), overall mean percentage deviation (MPD%), and mean absolute deviation (MAD). According to these parameter results, the best two methods (CAM-B3LYP and HSEh1PBE) were selected to save computational cost and time in determining

other structure-property parameters (the electronic transition and nonlinear linear optical parameters). Vibrational wavenumbers were determined using potential energy distribution (PED) analysis via the VEDA program [49, 50]. Additionally, NBO [51] analysis was conducted to elucidate the complex's coordination environment and intermolecular interactions. To investigate the electronic transitions of the Cd(II) complex, the electronic absorption wavelengths (λ_{abs}) and oscillator strengths (f), and transition dipole moments were obtained at the conductor-like polarizable continuum model (CPCM) [52] in ethanol by means of time-dependent DFT (TD-DFT). Frontier molecular orbitals (FMOs) playing an essential role in electronic transitions were identified using the SWizard [53] program, while the percentage contributions from individual atoms/atomic groups to these orbitals were quantified with the Chemissian [54] program. The static and dynamic (frequency-dependent, λ=514 nm) linear optical properties, including refractive index (n), isotropic polarizability, $<\alpha(0;0)>/<\alpha(-\omega;\omega)>$, and anisotropic polarizability, $(\Delta\alpha(0;0)/\Delta\alpha(-\omega;\omega))$, were computed at the DFT/CAM-B3LYP and HSEh1PBE methods. The static and dynamic second-order nonlinear optical susceptibility tensor components $(<\beta(0;0,0)>/<\beta(-\omega;\omega,0)>$ relevant to the electro-optic Pockels effect, and $<\beta(-2\omega;\omega,\omega)>$ corresponding to second harmonic generation (SHG) of the Cd(II) complex were computed at the same DFT levels. Furthermore, the static and dynamic third-order nonlinear optical (NLO) susceptibility tensor components $(<\gamma(0;0,0,0)>/<\gamma(-\omega;\omega,0,0)>$ corresponding to the quadratic electro-optic Kerr effect, and $<\gamma(-2\omega;\omega,\omega,0)>$ associated with DC electric-field-induced second harmonic generation (EFISHG) of the Cd(II) complex were calculated at the mentioned DFT levels. The static and dynamic linear and nonlinear optical properties, as well as global chemical reactivity descriptors, were evaluated using the equations provided in the Supplementary Material. Additionally, the stabilization energies $E^{(2)}$ for the NBO analysis were computed according to the corresponding equation presented in the Supplementary Material.

To illustrate the correlation between the selected DFT levels (B3PW91, B3LYP, CAM-B3LYP, ωB97XD, and HSEh1PBE) and experimental data for structural parameters, linear correlation coefficients (R^2), overall mean percentage deviation (MPD%), and mean absolute deviation (MAD) were examined using the equations provided in the Supplementary Material.

2.4 Docking details

A molecular docking investigation was conducted using the AutoDock4 tool [55] through the graphical user interface AutoDockTools (ADT1.5.7) [56] to investigate the protein-ligand interactions of the produced Cd(II) complex. The target protein, S. *cerevisiae* isomaltase, PDBID: 3A4A, was selected from the Protein Data Bank as rigid. PDB files for the Cd(II) complex and genistein, optimized at the CAM-B3LYP level using the Gaussian 16W program, were prepared for docking. ADT1.5.7 was utilized to assign Kollman charges, define rotatable bonds, and merge non-polar hydrogen atoms with carbon atoms. All calculations for flexible docking of the complex and target were fulfilled by using the Lamarckian genetic algorithm (LGA) method [57]. The grid and docking parameter files in PDBQT format for both the target and ligand (target.pdbqt, ligand.pdbqt) were prepared using AutoDock 4.2. AutoGrid 4 was used to define the docking region. AutoGrid 4 was used to define the docking area. The grid box dimensions were set at various points to encompass the target binding site and allow sufficient space for the Cd(II) complex and genistein to move freely. A 3D affinity grid centered on the Cd(II) complex and genistein binding site was calculated with a grid point spacing of 1.0 Å for each of the following atom types: (a) receptor (protein): A (aromatic C), C, Ca, HD, N, OA, SA, and (b) ligand: A, C, NA, N, SA. For the Cd(II) complex, Cd was included, while only A and OA were considered for genistein, along with electrostatic (e) and desolvation (d) terms. The following docking parameters were applied: Population size of 150, mutation rate of 0.02, elitism set to 1, crossover rate of 0.8, local search rate of 0.06, and 2,500,000 energy evaluations. The final docked conformations were obtained with a root mean square deviation (RMSD) tolerance of 2 Å.

Cd(II) complex: The grid points in the x, y, and z dimensions were set to 110, 108, 92 with the grid box center coordinates at 21.276 − 0.752 18.634.

Genistein [58]: The grid points in the x, y, and z dimensions were set to 60, 60, 60, with the grid box center coordinates at 21.831, − 0.612, 18.719.

The docking outcomes obtained were used to interpret the relative performance of the complexes in terms of stabilization and binding energy. The

Discovery Studio 4.0 software [59] was used to visualize 2D and 3D structures of the interactions between the Cd(II) complex's ligands and amino acid residues. The conformation Root Mean Square Deviation (RMSD) between the native alpha-D-glucose ligand and the re-docked co-crystallized ligand was evaluated based on structural alignment in a validation study to verify the acceptability of the chosen docking parameters. The RMSD value of 0.446 Å indicated that the chosen docking parameters were appropriate [58]. The Cd(II) combination and genistein were then docked onto the active region of the α-glucosidase homology model using these improved parameters.

3 Results and discussion

3.1 The analysis of the complex structure

Single-crystal X-ray diffraction analysis was carried out to determine the molecular and crystal structure of the Cd(II) complex. The refinement crystal parameters for Cd(II) complex are presented in Table 1. A suitable colorless crystal was selected and mounted on a diffractometer, and data were collected at room temperature (293 K) using Mo Kα radiation (λ = 0.71073 Å). The compound crystallizes in the monoclinic crystal system with space group $P2_1/c$. The unit cell parameters were determined to be a = 6.7618(4) Å, b = 10.9687(5) Å, c = 18.2000(11) Å, with β = 92.828(5)°, and α = γ = 90°, resulting in a unit cell volume of 1348.22(13) Å^3. The crystal used for data collection had dimensions of 0.11 × 0.08 × 0.07 mm^3. A total of 10,624 reflections were measured in the 2θ range of 2.9 to 25.1°, from which 2378 were independent (R_{int} = 0.055). The structure was solved using direct methods and refined by full-matrix least squares on F^2. Final refinement converged with R_1 = 0.085 for observed reflections [I > 2σ(I)] and wR_2 = 0.191 for all data, with a goodness of fit (S) of 1.17. The calculated density of the crystal was 2.096 g·cm^{-3}, and the absorption coefficient (μ) was 2.03 mm^{-1}. The final difference Fourier map revealed the largest residual electron density peak and hole to be +2.45 and − 0.74 e·Å^{-3}, respectively.

The crystal structure parameters for Cd(II) complex determined by the X-ray diffraction method are presented in Table 2. The 2D structure and 3D single crystal structure of Cd(II) complex are presented in Fig. 1. The polymeric structure of the Cd(II) complex imposes several limitations on theoretical calculations.

Table 1 Crystal data and structure refinement parameters for the Cd(II) complex

	Cd(II) complex
CCDC Number	2076519
Chemical formula	$C_{12}H_6CdCl_2N_2O_4$
Formula weight	425.49
Crystal color	Colorless
Crystal system	Monoclinic
Space group	$P2_1/c$
Temperature (K)	293
Radiation type	Mo Kα
Wavelength (Å)	0.71073
Crystal size (mm)	0.11 × 0.08 × 0.07
h, k, l	− 7→8, − 13→13, − 21→21
a (Å)	6.7618 (4)
b (Å)	10.9687 (5)
c (Å)	18.2000 (11)
α (°)	90°
β (°)	92.828(5)°
γ (°)	90°
V (Å^3)	1348.22(13)
Z	4
F(000)	824
Density (g cm^{-3})	2.096
μ (mm^{-1})	2.03
θ range (°)	2.9–25.1°
Measured refls.	10624
Independent refls.	2378
R_{int}	0.055
S	1.17
R1/wR2	0.085/0.191
max/min (eÅ^{-3})	2.45/ − 0.74

Because the crystal structure consists of an infinite coordination network, only a portion of the unit cell, typically centered around a single Cd ion with a hexa-coordination sphere, can be considered in molecular DFT approaches. The polymeric crystal structure of the Cd(II) complex necessitates the application of fragment-based models to render the theoretical calculations computationally feasible. Nevertheless, this simplification inevitably limits the representation of long-range interactions, the intrinsic electronic structure, and collective crystal effects. Therefore, the DFT outcomes should be regarded primarily as qualitative insights, while their quantitative reliability should be interpreted with caution. For the Cd complex obtained in the polymeric structure, theoretical calculations

Table 2 The experimental and theoretical geometrical parameters of the Cd(II) complex

Parameters	XRD	B3PW91	B3LYP	CAM-B3LYP	ωB97XD	HSEh1PBE
Bond lengths (Å)						
Cd1—O1	2.258 (5)	2.252	2.257	2.209	2.209	2.238
Cd1—O4	2.265 (5)	2.252	2.257	2.209	2.209	2.238
Cl1—C6	1.713 (8)	1.804	1.815	1.800	1.799	1.797
Cl1—C12	1.722 (8)	1.804	1.815	1.800	1.799	1.797
O1—C1	1.265 (9)	1.303	1.306	1.313	1.314	1.300
O4—C7	1.288 (9)	1.303	1.306	1.313	1.314	1.300
O2—C1	1.241 (9)	1.274	1.278	1.262	1.260	1.272
O3—C7	1.226 (9)	1.274	1.278	1.262	1.260	1.272
N1—C6	1.334 (10)	1.323	1.325	1.321	1.322	1.322
N2—C12	1.324 (9)	1.323	1.325	1.321	1.322	1.322
N1—C2	1.360 (8)	1.351	1.354	1.349	1.351	1.348
N2—C8	1.345 (9)	1.351	1.354	1.349	1.351	1.348
R^2		**0.99010**	**0.98868**	**0.98633**	**0.98675**	**0.98996**
RMSD		**0.0413**	**0.0460**	**0.0449**	**0.0445**	**0.0393**
Bond angles (°)						
O1—Cd1—O4	99.4 (2)	95.8	96.2	95.9	97.6	97.8
C1—O1—Cd1	128.7 (5)	134.1	134.4	133.6	132.9	133.0
C7—O4—Cd1	128.8 (4)	134.1	134.4	133.6	132.9	133.0
C6—N1—C2	116.3 (6)	119.0	119.1	118.5	118.2	118.9
C12—N2—C8	116.9 (6)	119.0	119.1	118.5	118.2	118.9
O2—C1—O1	127.2 (7)	121.9	121.9	121.7	121.7	122.3
C3—C7—O4	126.4 (7)	121.9	121.9	121.7	121.7	122.3
N1—C6—Cl1	116.9 (6)	117.8	117.8	117.7	117.4	117.8
N2—C12—Cl2	116.4 (6)	117.8	117.8	117.7	117.4	117.8
C5—C6—Cl1	117.7 (6)	118.6	118.6	118.5	118.4	118.5
C11—C12—Cl2	119.7 (6)	118.6	118.6	118.5	118.4	118.5
C2—C3—C4	119.4 (7)	118.3	118.3	118.1	118.1	118.2
C8—C9—C10	119.0 (7)	118.3	118.3	118.1	118.1	118.2
R^2		**0.86181**	**0.85623**	**0.86655**	**0.87377**	**0.87863**
RMSD		**2.79**	**3.30**	**3.24**	**3.11**	**2.73**
Dihedral angles (°)						
Cd1—O1—C1—O2	− 1.1 (12)	9.6	8.8	13.3	13.8	10.7
Cd1—O4—C7—O3	− 15.8 (11)	9.6	8.8	13.3	13.8	10.7
Cd1—O1—C1—C2	178.1 (4)	− 170.1	− 170.8	− 166.1	− 165.7	− 168.9
Cd1—O4—C7—C8	162.4 (4)	− 170.1	− 170.8	− 166.1	− 165.7	− 168.9
C6—N1—C2—C1	180.0 (6)	179.5	179.5	179.6	179.5	179.4
C12—N2—C8—C7	− 177.9 (6)	179.5	179.5	179.6	179.5	179.4
O2—C1—C2—N1	13.0 (9)	173.9	173.5	172.4	173.4	171.6
O3—C7—C8—N2	− 174.5 (6)	173.9	173.5	172.4	173.4	171.6
C2—N1—C6—Cl1	− 178.6 (5)	179.5	179.5	179.6	179.7	179.3
C8—N2—C12—Cl2	175.9 (5)	179.5	179.5	179.6	179.7	179.3
O2—C1—C2—C3	13.4 (10)	− 6.5	− 6.9	− 7.9	− 7.1	− 8.9
O3—C7—C8—C9	7.1 (10)	− 6.5	− 6.9	− 7.9	− 7.1	− 8.9

R^2 and RMSD are defined as the linear correlation coefficient and overall root mean square deviation for bond lengths and angles, respectively

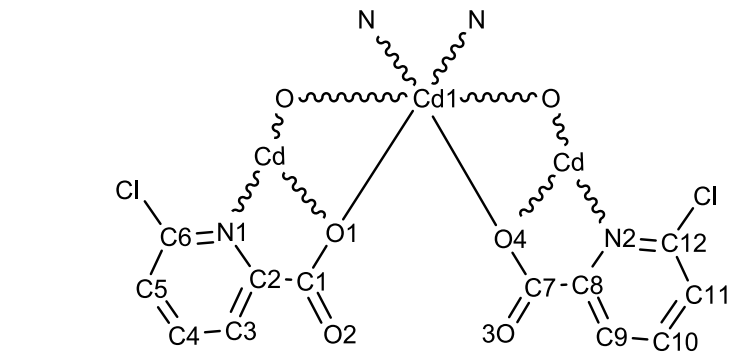

(a)

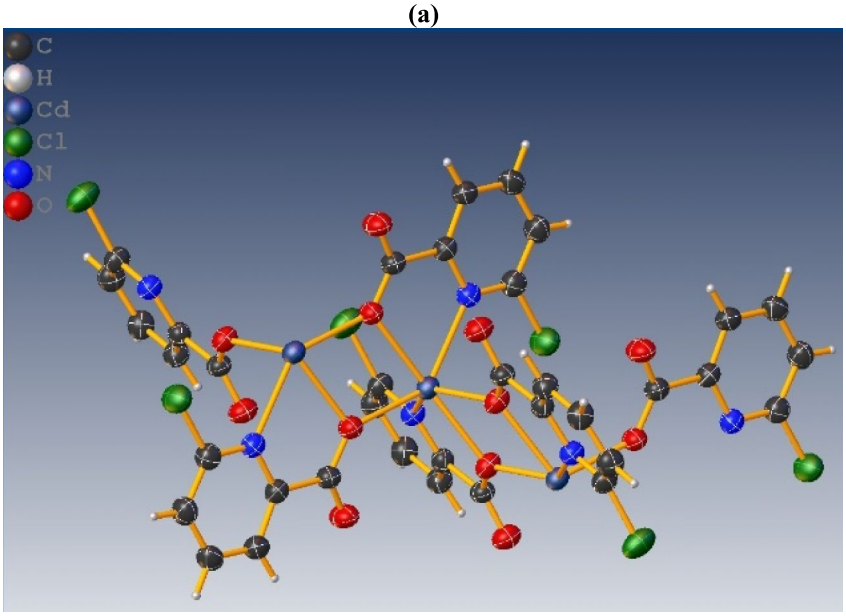

(b)

Fig 1 **a** 2D structure **b** 3D single crystal structure of the Cd(II) complex

were performed to obtain an optimal structure showing the six-membered coordination geometry around the central metal ion. In all selected DFT methods, the Cd complex was obtained in a distorted octahedral geometry with the Cd ion forming a five-membered heterocyclic ring with the N, O atoms of two 6-chloropicolinate ligands and providing monodentate coordination with the O atoms of the other two 6-chloropicolinate ligands. Table 2 compares the geometrical parameters of the Cd(II) complex optimized by various DFT methods (B3PW91, B3LYP, CAM-B3LYP, ωB97XD, and HSEh1PBE) against the crystal structure (XRD). XRD data for Cd–O bonds between the Cd ion and O atom of the carboxylate group are 2.258–2.265 Å, while theoretical methods give values in the range of 2.209–2.257 Å. The lowest values were obtained in CAM-B3LYP and ωB97XD, while the highest values were obtained in B3LYP. Although the Cl–C bonds within the ring were experimentally obtained at ~1.71–1.72 Å, they were found to be slightly larger (~1.80–1.81 Å) in DFT calculations. As for the results for C=O and C–O bonds belonging to the carboxylate group, the bond length of C=O (O2–C1, O3–C7) was obtained experimentally as 1.226–1.241 Å, with minor differences of ~1.26–1.28 Å from the theoretical results. The bond length of C–O (O1–C1, O4–C7) was obtained experimentally as 1.265–1.288 Å, with slightly longer theoretical values. As expected, the C-O bonds in coordination with the Cd ion were observed to be slightly longer. In N–C bonds belonging to the ring, the experimental and theoretical values are generally very consistent, with minimal deviations (<0.01 Å). In the bond length comparison, the lengths given by the experimental (XRD) and five theoretical methods (DFT) for each bond are shown, while for some bonds, especially the Cl–C and Cd–O bonds, the theoretical

data give longer results than the XRD. The O–Cd–O angle between the O atoms of the carboxylate group of the 6-chloropicolinate ligand and the Cd ion was experimentally calculated as 99.4°, and the smaller theoretical values obtained in the range of 95.8–97.8° indicate that the coordination geometry is slightly tighter. The C–O–Cd bond angles between the carboxylate groups and the Cd ion were experimentally obtained as ~128.7°, while the theoretical values were calculated in the range of 132.9–134.4°. In the pyridine ring, the theoretical results of the N–C–C angles show that they are approximately 2–3° larger than the experimental ones.

The most compatible values in terms of R^2 in bond lengths were obtained in the B3PW91 (0.99010) method, while other methods also reached very close results between 0.98633 and 0.98996. The RMSD analysis shows how close each theoretical method is to the XRD data in terms of bond lengths. The lower the RMSD, the better the method models. In this respect, the HSEh1PBE method shows the best modeling of bond lengths, while B3LYP has the highest deviation for this complex. In terms of R^2 results of the bond angles, the highest result was found in the HSEh1PBE (0.87863) method, while the lowest was obtained in B3LYP (0.85623), and no major differences were observed between them and other methods. In the comparison of the bond angles given by the XRD measurements and theoretical methods, according to the RMSD data, HSEh1PBE and ωB97XD are the most accurate methods for bond angles, while B3LYP can be stated as the method with the highest deviation in this group.

While B3PW91 gives the best results in terms of bond lengths, HSEh1PBE and ωB97XD methods provide the best agreement in bond angle parameters. This analysis can be a guide when deciding which functional is more appropriate to use in structure optimization. In this study, HSEh1PBE and ωB97XD methods stood out for the overall results closest to the crystal structure.

Hyperconjugative effects were evaluated via $E^{(2)}$ energies using second-order perturbation theory [60, 61] in the framework of natural bond orbital (NBO) analysis. Moreover, the $E^{(2)}$ stabilization energies calculated at the DFT/CAM-B3LYP and ωB97XD/LanL2DZ levels provide insights into the coordination geometry of the metal ion within the complex, its conjugative interactions, and the overall strength of bonding interactions. Table S1 presents the $E^{(2)}$ stabilization energies, which range from 10.66 to 56.31 kcal/mol at the CAM-B3LYP level and from 10.80 to 58.39 kcal/mol at the ωB97XD level. The n→n* interactions obtained at 10.80 and 10.96 kcal/mol at the ωB97XD level are attributed to the interaction between the lone pair (n) orbitals of the O atoms of 6-ClPCA and the anti-lone pair (n*) orbitals of the Cd(II) ion. These results are in agreement with the previously reported Cd(II) complex of 6-methylpicolinate (6-Mepic) ligand [26]. On the other hand, the LP(1)O1/O4→σ*(Cd1–O1)/(Cd1–O4) interactions belonging to the bonding between 6-ClPCA and Cd ion appeared at the values of 25.13 (CAM-B3LYP), 26.74 kcal/mol (ωB97XD level), as seen in Table S1. The electronic configuration of Cd(II) ion is [core]$5s^{(0.24)}4d^{(9.93)}5p^{(0.32)}$ with 36.00000 core electrons, 10.49338 valence electrons, and 0.00684 Rydberg electrons calculated at ωB97XD level. The natural charge of the Cd(II) ion, calculated as 1.49978e, deviates from the nominal 2+ oxidation state, indicating a partial charge transfer from the Cd(II) center to the coordinated 6-ClPCA ligands and suggesting some covalence in the metal-ligand interactions. NBO analysis revealed that the structural stabilization of the complex is attributed to interactions between bonding and antibonding orbitals, delocalization among bonding pairs, and the coordination environment surrounding the metal ions.

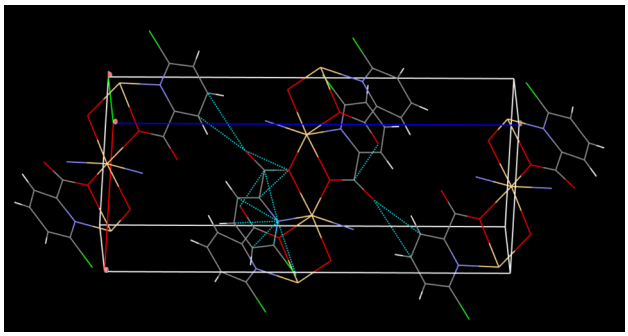

Fig 2 The crystal packing structure of the Cd(II) complex

Table 3 Hydrogen-bond parameters for the Cd(II) complex (Å and °)

D—H· · ·A	D—H	H···A	D···A	D—H···A	Symmetry codes
C9—H9···O2^{iii}	0.93	2.50	3.130 (9)	125	(iii) $-x$, $-y+3/2$, $z-1/2$

The crystal packing structure of the Cd(II) complex exhibits intermolecular C–H···O hydrogen bonding interactions, where hydrogen atoms from C–H units engage with oxygen atoms belonging to carboxylate groups in the 6-ClPCA ligands (see Fig. 2 and Table 3).

3.2 The analysis of the vibrational frequencies

The vibrational frequencies of the Cd(II) complex were characterized by using experimental IR spectra and the various DFT/B3PW91, B3LYP, CAM-B3LYP, ωB97XD, and HSEh1PBE levels. FTIR spectra for the 6-ClPCA and Cd(II) complex are recorded in the middle IR region (see Fig. 3). The experimental vibrational modes and corresponding theoretical ones were assigned by using PED% analysis for the CAM-B3LYP level, as can be seen in Table 4. The remarkable differences/similarities between experimental and theoretical modes by utilizing the λ, RMS, MAD, MPD%, and R^2 values associated with the 38 observed vibrational frequencies were analyzed and given in Table 4. Based on the outcomes associated with these parameters, the DFT method that showed the best fit was the HSEh1PBE level obtained at 0.9463, 23.497 cm^{-1}, 62.809 cm^{-1}, 5.3745%, and 0.99875, respectively. In general, no major differences were observed between the selected methods. A similar comparison of experimental and different DFT levels vibrational data was made for a Cu(II) complex [5]. Among the methods compared, CAM-B3LYP yielded slightly higher RMS and MAD values compared to functionals like M06L and TPSSTPSS for that particular complex. In current study, the RMS and MAD values for B3PW91/, B3LYP/, CAM-B3LYP/, ωB97XD/, and HSEh1PBE/LanL2DZ levels were calculated at 24.232/56.012 cm^{-1}, 32.268/48.94 cm^{-1}, 27.138/71.524 cm^{-1}, 26.521/71.566 cm^{-1}, 23.497/62.809 cm^{-1}, respectively. On the other hand, the MPD% and R^2 results demonstrate the minor differences between selected DFT levels due to the characteristics of the methods. The results of the optimum scaling factor (λ)/RMS parameters in this study show that they are comparable with the results obtained for various compounds in different DFT methods and basis sets [5, 33, 62–67]. The R^2 parameters, which show the degree of agreement among the theoretical frequencies obtained by multiplying with the λ values with their corresponding experimental ones, were obtained as the comparative performance of the DFT methods B3LYP<ωB97XD<CAM−B3LYP<B3PW91<HSEh1PBE for 38 vibration modes. The RMS values of the evaluated DFT functionals are in decreasing order as B3LYP>CAM−B3LYP>ωB97XD>B3PW91>HSEh1PBE. The MAD values were obtained as ωB97XD>CAM−B3LYP>HSEh1PBE B3PW91>B3LYP ranking from largest to smallest. As clearly seen from

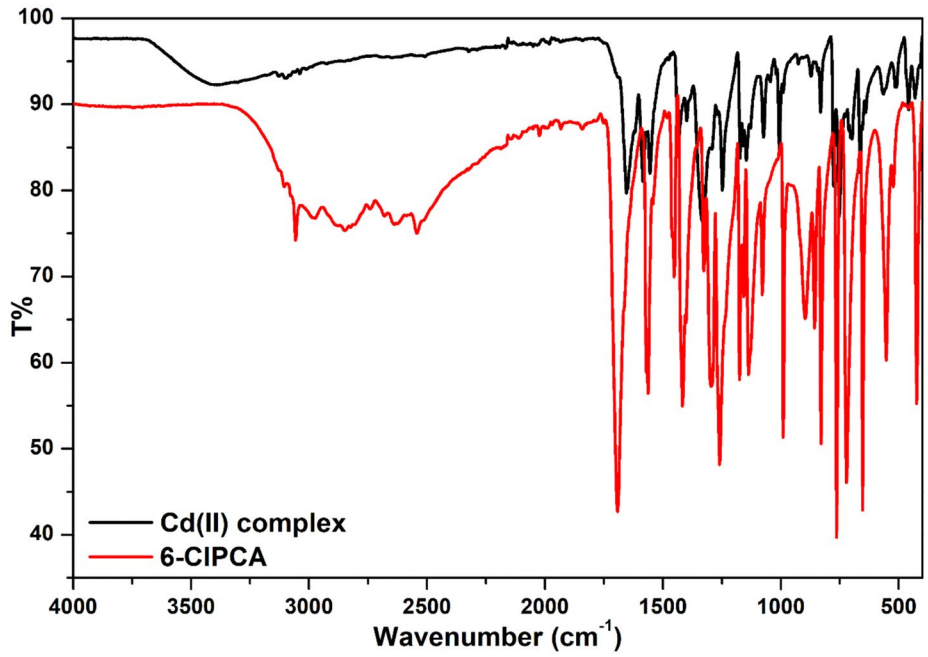

Fig 3 The experimental IR spectra for the Cd(II) complex and 6-ClPCA

Table 4 The experimental and corresponding theoretical vibrational frequencies for the Cd(II) complex

Assignments via PED% (with CAM-B3LYP)	FT–IR (cm^{-1})	B3PW91 Scaled freq[a]	B3LYP	CAM-B3LYP	ωB97XD	HSEh1PBE
υ CH 86%	3129	3121	3088	3085	3095	3114
υ CH 77%	3096	3086	3051	3050	3062	3079
υ CH 77%	3038	3086	3051	3050	3062	3079
υ CC 36%	1655	1564	1537	1571	1571	1567
υ NC 22%	1585	1550	1524	1556	1555	1553
υ NC 22%	1568	1550	1524	1556	1554	1553
υ CC 38%	1555	1540	1514	1547	1549	1544
υ OC 73%	1441	1434	1405	1486	1502	1439
υ OC 40%	1432	1424	1400	1441	1444	1428
υ OC 24%+ β HCC 48%	1399	1388	1369	1386	1391	1387
υ OC 24%	1332	1316	1288	1286	1291	1317
υ NC 20%	1247	1264	1233	1228	1233	1263
β HCC 48%	1173	1156	1144	1144	1150	1155
β HCC 48%	1160	1154	1143	1143	1150	1154
υ OC 22%	1146	1144	1129	1128	1130	1142
υ OC 22%+ β HCC 22%	1129	1140	1127	1118	1122	1137
β HCC 21%	1073	1098	1082	1101	1103	1100
β HCC 39%	1045	1053	1041	1045	1049	1051
υ CC 38%+ β HCC 30%	1020	1043	1031	1039	1043	1042
τ HCCC 66%	1006	998	993	1011	1004	997
τ HCCC 53% + τ HCCC 22%	990	992	988	1006	998	991
τ HCCC 86%	926	921	916	931	927	920
τ HCCN 15% + τ HCCC 66%	873	914	909	931	925	913
τ HCCC 46%	844	814	807	823	819	815
τ HCCC 47%	832	814	807	823	819	815
υ CC 24% + υ ClC 20%	776	806	794	804	803	809
τ HCCC 10%	753	746	738	746	745	745
τ HCCC 20% + γ NCCC 10%	712	742	734	745	743	742
τ CNCC 21% + γ OCOC 32%	705	694	686	701	699	695
β CCC 20%	664	662	655	660	660	662
β CCC 28%	654	653	646	644	644	653
β OCO 28%	640	618	613	620	621	617
β OCO 48%	565	582	578	571	564	584
β NCC 12% + β CCO 34%	516	522	517	525	524	525
γ ClCNC 21%	510	498	492	499	499	496
γ ClCNC 11% + γ CCNC 10%	459	496	490	495	495	493
γ CCNC 44%	432	432	430	437	434	431
γ CCCC 36% + γ CCNC 12%+ γ NCCC 15%	411	407	402	415	416	410
λ		**0.9524**	**0.9467**	**0.9379**	**0.9390**	**0.9463**
RMS (cm^{-1})		**24.232**	**32.268**	**27.138**	**26.521**	**23.497**
MAD (cm^{-1})		**56.012**	**48.946**	**71.524**	**71.566**	**62.809**
MPD%		**5.1006**	**4.5323**	**6.6834**	**6.5688**	**5.3745**
R^2		**0.99865**	**0.99844**	**0.99854**	**0.99848**	**0.99875**

λ, RMS, MAD, MPD%, and R^2 are defined as the optimal scaling factor, overall root mean square deviation, mean absolute deviation, overall mean percentage deviation, linear correlation coefficients for vibrational frequencies, respectively

Table 4, it is found that B3LYP exhibits lower performance compared to the other functionals for vibration frequencies, while HSEh1PBE gives better results.

The FT-IR spectral bands were assigned with the help of potential energy distribution (PED) percentages, particularly using the CAM-B3LYP method, and the results were benchmarked across several functionals (B3LYP, B3PW91, ωB97XD, and HSEh1PBE). The most intense and characteristic bands in the high frequency region (3100–3030 cm^{-1}) were attributed to aromatic C–H stretching vibrations, which are consistent with those reported by Avcı et al. for various metal(II) complexes (with those observed in 6-methylpyridine-2-carboxylic acid complexes) [26]. The shifts in these bands between the experimental and calculated values are within an acceptable range (RMS ~24–32 cm^{-1}), confirming the reliability of the selected theoretical methods. The bands in the region of ~1655–1550 cm^{-1} were attributed to C=C and C=N stretching vibrations, indicating strong coordination between the ligand and the metal center. These assignments are consistent with the findings from similar Zn(II), Cu(II), and Co(II) complexes reported in the literature [1, 3, 4]. In particular, the shift towards lower wavenumbers observed in the υ(C=O) mode confirms the involvement of the carboxylate oxygen in coordination, which is consistent with the metal–ligand bonding modes proposed in comparable systems. Furthermore, the existence of torsional and out-of-plane deformation modes between 1000 and 400 cm^{-1} was correctly predicted by DFT calculations and was observed to be similar to those observed in structurally related metal-picolinate complexes [1, 3, 4]. These low-frequency vibrations promote the formation of a stable coordination environment around the Cd(II) center. It can be stated that the differences in IR bands in metal(II) complexes [1, 3, 4, 68] vary depending on the characteristics of the electron-donating (-CH_3) and electron-accepting substituents (-Cl and -Br) at the 6-position in picolinate derivatives.

In conclusion, vibrational analysis strongly supports the proposed coordination structure and binding properties of the Cd(II) complex. The consistency of the data with structurally similar systems further validates the coordination behavior of the ligand and the computational methodology used.

3.3 The analysis of the electronic transitions and molecular reactivity parameters

The UV-Vis and optical band gap spectra in ethanol of the Cd(II) complex are given in Fig. 4a,b. Furthermore, TD–CAM-B3LYP and HSEh1PBE/LanL2DZ levels were applied to obtain the electronic transition dipole moments, oscillator strengths, and absorption wavelengths. Using the SWizard [53] and

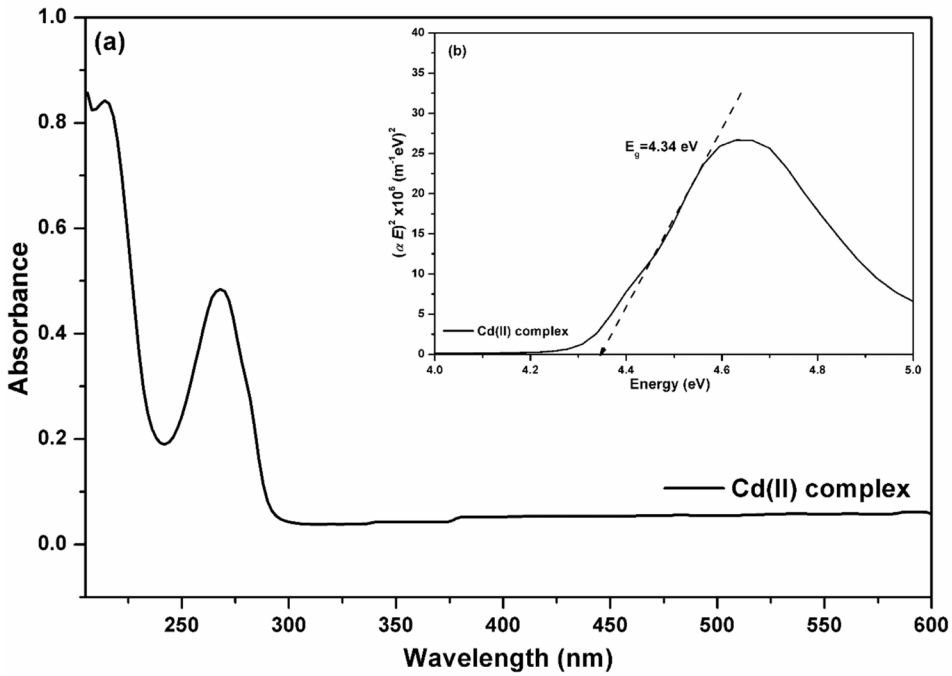

Fig 4 **a** The UV-Vis spectrum and **b** the optical band gap energy graph for the Cd(II) complex in ethanol

Table 5 The experimental and theoretical electronic absorption wavelengths/transitions, oscillator strengths, and transition dipole moments for the Cd(II) complex

Solvent	Exp. λ (nm)	Theoretical results			
		λ (nm)	Osc. strength	μ_{eg} (D)	Major contributions determined via SWizard//Chemissian program 6-ClPC: 6-Chloropicolinate; Cd: Cadmium
TD–CAM-B3LYP/LanL2DZ/CPCM/Ethanol					
	268	269	0.0058	0.577	32% H→L+4 [6-ClPC(98%)+Cl(2%)→6-ClPC(100%)]
					20% H−3→L+3 [6-ClPC(96%)+Cl(3%)→6-ClPC(100%)]
		240	0.2169	3.331	27% H−1→L+3 [6-ClPC(73%)+Cl(27%)→6-ClPC(100%)]
					22% H−2→L+4 [6-ClPC(73%)+Cl(27%)→6-ClPC(100%)]
	214	212	0.0364	1.281	53% H→L+1 [6-ClPC(98%)+Cl(2%)→6-ClPC(98%)+Cd(2%)]
					10% H→L+4 [6-ClPC(98%)+Cl(2%)→6-ClPC(100%)]
TD–HSEh1PBE/LanL2DZ/CPCM/Ethanol					
	268	270	0.0098	0.751	67% H→L+1 [6-ClPC(94%)+Cl(6%)→6-ClPC(98%)]
					19% H→L+4 [6-ClPC(94%)+Cl(6%)→6-ClPC(100%)]
		249	0.0374	1.403	58% H−2→L+4 [6-ClPC(95%)+Cl(4%)→6-ClPC(100%)]
	214	221	0.0038	0.421	40% H−2→L+6 [6-ClPC(95%)+Cl(4%)→6-ClPC(96%)+Cl(3%)]
					27% H−1→L+5 [6-ClPC(94%)+Cl(4%)+Cd(2%)→6-ClPC(97%)+Cl(3%)]

Chemissian [54] programs, the contributions from molecular orbitals among ligands, the –Cl atom, and the Cd ion were examined for the Cd(II) complex (see Table 5). As illustrated in Fig. 4a, two prominent absorption peaks at 268 and 214 nm are associated with ligand-to-metal/metal-to-ligand charge transfer and intra-ligand π→π transitions. The corresponding theoretical bands are obtained at 269 and 212 nm by using TD–CAM-B3LYP/LanL2DZ level, respectively. According to the TD–CAM-B3LYP results, the contributions of the selected 6-ClPC ligand to the HOMO and LUMO levels, excluding the Cl atom at the 6-position, vary from 73 to 98% (for HOMO) and from 98 to 100% (for LUMO). In addition, the contribution of the Cl atom was determined as 27% only at the HOMO-1 and HOMO-2 levels. The electronic absorption bands at 269, 240, and 212 nm were obtained at oscillator strengths f = 0.0058, 0.2169, 0.0364 and transition dipole moments μ_{eg} = 0.0537, 3.331, and 1.281 D at the TD–CAM-B3LYP level in ethanol. These bands represent the electronic transitions induced by the excitations 32% H→L+4/20% H−3→L+3, 27% H−1→L+3/22% H−2→L+4, and 40% H→L+1/27% H→L+4, respectively. Considering the d^{10} electron configuration of the Cd(II) ion, ligand-ligand charge transfer (LLCT) transitions are more pronounced, while metal-ligand charge transfer (MLCT) transitions are detected at very low levels. It can be noted that these results are consistent with those observed in various metal(II) complexes of 6-bromo/chloro/methyl-pyridine-2-carboxylic acid made previously [1, 3, 4]. In these bands, the shifts are as expected in complexes formed by ligands with electronegative chlorine and bromine atoms and electron-donating methyl groups at the 6-position.

The most significant FMOs involved in the electronic transition of the Cd(II) complex in ethanol, calculated at the CAM-B3LYP level, are shown in Fig. 5. The HOMO is mainly centered on the 6-ClPC ligand, while the LUMO is localized on the metal ion and its environment. As shown in Fig. 5, the electron density in the HOMO is mainly concentrated on two 6-ClPC ligands, whereas in the HOMO−3 it is distributed over the other similar ligands. It is clearly seen from the results in Fig. 5 and Table 5 that at lower HOMO and higher LUMO levels of the Cd(II) complex, the electron density is mostly partially or completely localized on the 6-ClPC ligands and the intra-ligand charge transfer is more dominant.

Eq. (1) is employed to determine the energy band gap and type of optical transition, in accordance with the Tauc and Menth model [3, 69].

$$(\alpha h\nu) = A(h\nu - E_g)^m \quad (1)$$

In this equation, when the transmittance (T) and the length of the cuvette (d) are taken as 10 mm, the absorption coefficient (α) is found by $\alpha = -2.303 \log T/d$ [3, 70]. For allowed transitions, the

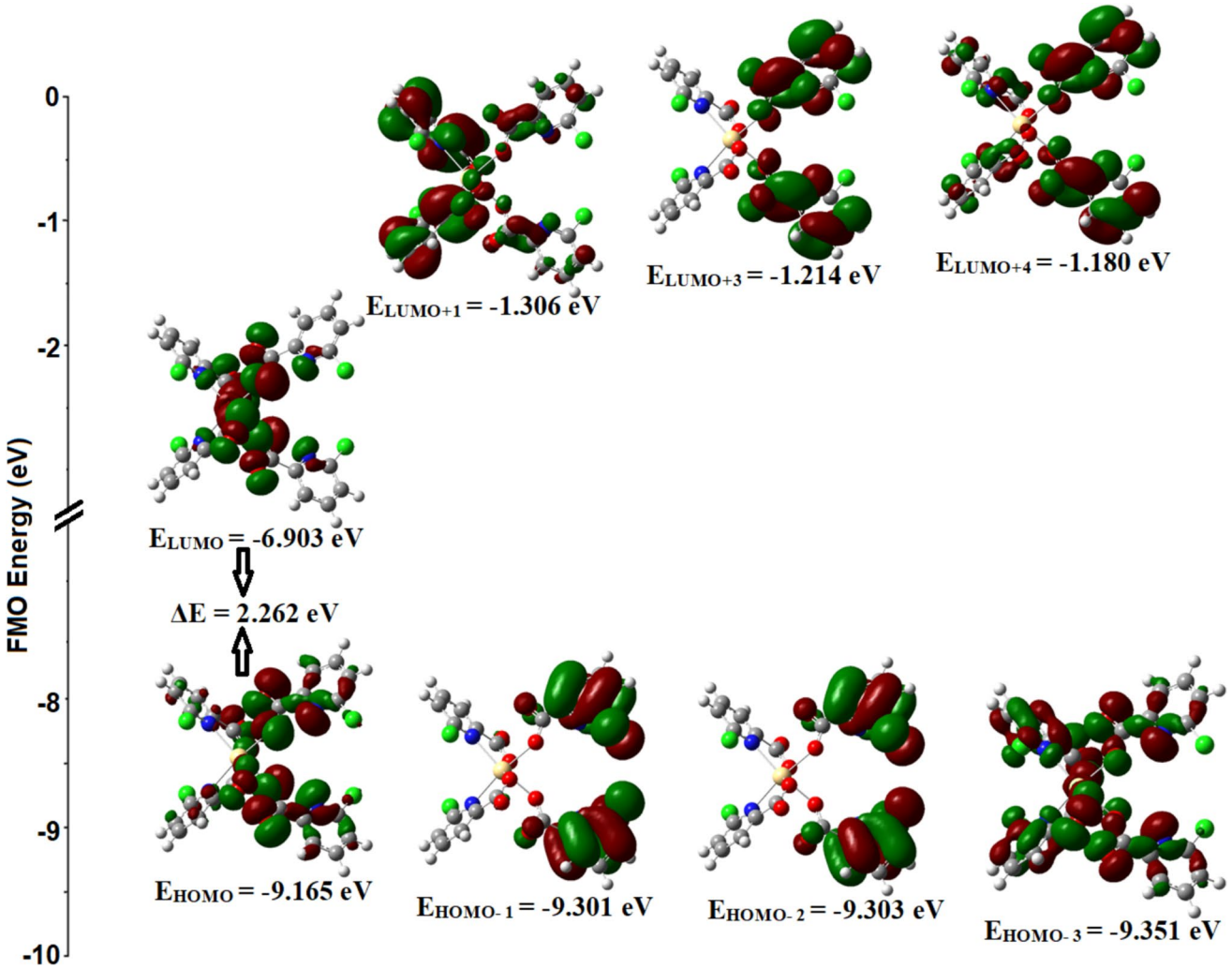

Fig 5 Main FMOs involved in electronic transitions of the Cd(II) complex revealed by DFT/CAM-B3LYP calculations in ethanol

exponent m is assigned a value of 1/2 for direct and 2 for indirect transitions, respectively. Since the results for the Cd(II) complex are consistent with the direct transition (m=1/2), the optical band gap energy value is found to be 4.34 eV by extrapolating the linear part of the graph relating $(\alpha h\nu)^2$ against $(h\nu)$ to $(\alpha h\nu)^2=0$ in Fig. 4b.

Frontier Molecular Orbital (FMO) analysis, which considers the energies of the HOMO and LUMO orbitals, allows for the estimation of molecular properties such as hardness, softness, and electrophilicity/nucleophilicity indices-key parameters for interpreting chemical reactivity and potential biological activity. The experimental band gap energy (E_g) obtained at 4.34 eV for the Cd(II) complex (see Fig. 4b) and the corresponding value in ethanol were calculated as 2.262 eV from the FMO energies at the CAM-B3LYP level. The band gap for the Cd(II) complex of 6-Mepic ligand was reported at 4.51 [26] by using HSEh1PBE level. The small differences in these results indicate the effect of the properties of the electron acceptor/donor (Cl/methyl group) groups at the 6-position in the coordination compounds on the complex structure.

Using FMO energies at the CAM-B3LYP level, the values of electronegativity (χ), chemical hardness (η), chemical softness (S), electrophilicity (ω), and nucleophilicity (φ) were determined as 8.034 eV, 1.131 eV, 0.884 eV^{-1}, 28.53 eV, and 0.035 eV^{-1}, respectively. The results calculated in the gas phase using other methods are presented in Table S2. The differences between the χ, η, and S values obtained here and the values given for the Cd complex of the 6-Mepic ligand [26] can be interpreted as the change resulting from the

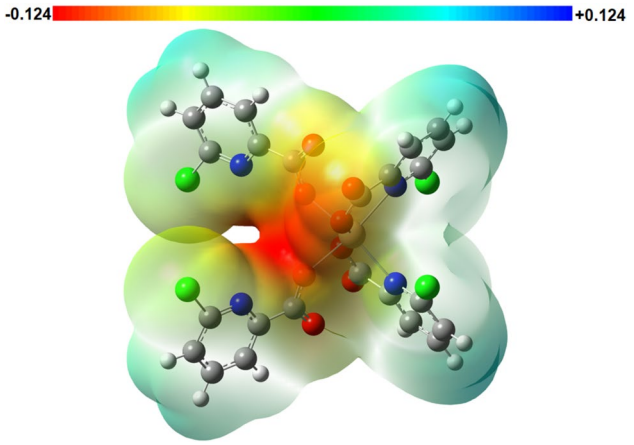

Fig 6 Molecular electrostatic potential (MEP) surfaces for the Cd(II) complex obtained at DFT/CAM-B3LYP level in ethanol

ligand and coordination in the complex structure. The presence of electron acceptor/donor (Cl/methyl group) groups at the 6-position in coordination compounds reveals a significant change in the electrophilic properties of the complex structure.

Molecular electrostatic potential (MEP) surface analysis [71, 72] serves as an effective tool for predicting intermolecular interactions and molecular characteristics of systems like drug compounds and related analogues. Fig. 6 presents the MEP surface of the Cd(II) complex calculated using the CAM-B3LYP/LanL2DZ level. Fig. 6 shows that the red regions, indicative of electrophilic reactivity, are located on the uncoordinated electronegative oxygen atoms of the carboxylate groups in the 6-ClPCA ligands, whereas the blue regions, corresponding to nucleophilic reactivity, appear on the C–H bonds of the ligands.

3.4 Z–Scan study

The Z–scan technique is a sensitive measurement method that allows direct measurement of the nonlinear absorption coefficient [73, 74]. Using this technique, the third-order nonlinear refractive index (n_2) and nonlinear absorption coefficient (β) parameters of the ethanol solution of Cd(II) complex were calculated. An Argon-ion continuous laser with a wavelength of 514 nm was utilized as the source. The Gaussian profile laser beam was focused by a lens with a focal length of 200 mm into a cuvette containing a 10^{-4} M concentration solution to produce a beam waist size ω_0 of 65.5 μm. To minimize thermal lensing and phase transition effects, the incident laser power was carefully adjusted, and measurements were conducted under low-power, steady-state conditions, ensuring that the sample remained within the linear thermal response regime. To assess the repeatability and stability of the Z-scan results, each measurement was repeated several times under the same conditions. The normalized transmittance curves showed consistent behavior across all experiments. In order to minimize phase transition in the Z–scan experiment (Scheme 2), it is important to consider the sample as thin compared to the Rayleigh length. In this measurement, the fundamental requirement for sample thickness was satisfied since the Rayleigh length (Z_R) exceeded the sample thickness (L), with Z_R representing the diffraction length of the Gaussian beam. So as to change the incident intensity on the sample, light was shed on the sample between −3 mm and +3 mm at the focal point of the lens with z=0, and the associated closed-aperture (CA) and open-aperture (OA) transmittance measurements were fulfilled. The CA transmittance was recorded by detecting the beam transmitted through an aperture positioned in the far field, using a photodiode detector connected to a digital power meter. In the OA Z–scan configuration, the aperture is substituted with a lens to capture the entire laser beam transmitted through the sample. Figs. 7a and b display the Z–scan curves obtained in closed-aperture and open-aperture modes, respectively. The OA and CA Z–scan analyses of Cd(II) complex for NLO parameter determination are presented in Table 6.

The nonlinear refractive index (n_2) is employed to calculate the peak-to-valley transmittance difference ($\Delta T_{p\text{-}v}$), which correlates with the on-axis phase shift ($\Delta\Phi_0$) according to eq. (2).

$$\Delta T_{p-v} = 0.406(1-S)^{0.25}\left|\Delta\Phi_0\right| \tag{2}$$

Here, $S = 1 - \exp\left(-2r_a^2/\omega_a^2\right)$, r_a is thSe aperture radius, and ω_a is the transmittance of the linear aperture, defined depending on the beam radius in the aperture in the linear regime. By applying a fit of the data to the expression eq. (3) [74], the valuSe of $\Delta\Phi_0$ is obtained as − 0.04037.

$$T_{CA}(z,\Delta\Phi) \approx 1 + \frac{4\Delta\Phi x}{\left(x^2+1\right)\left(x^2+9\right)} \tag{3}$$

Here $x = \frac{z}{z_0}$

n_2 is obtained from the eq. (4).

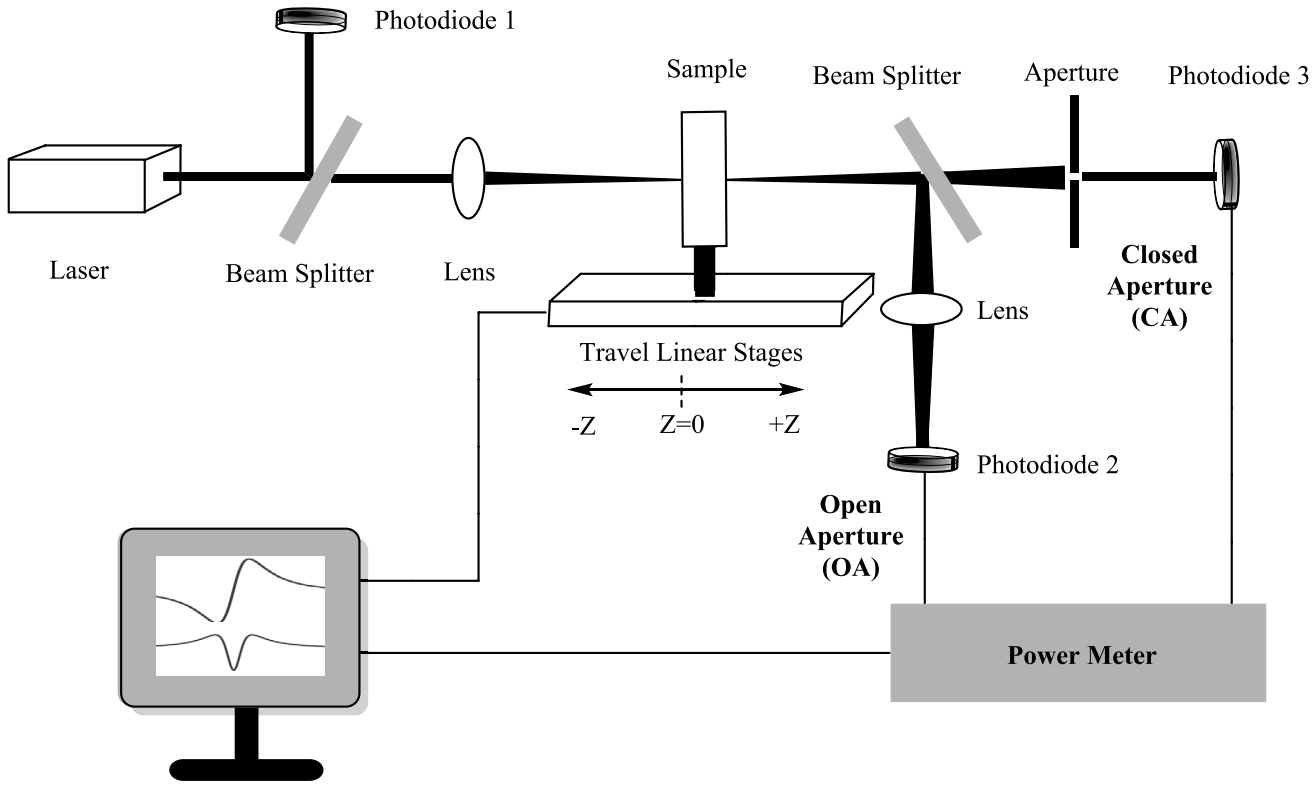

Scheme 2 The schematic representation of the Z–scan measurement technique for open and closed aperture

$$n_2 = \frac{\Delta\Phi_0 \lambda}{2\pi I_0 L_{eff}} \tag{4}$$

Here, the laser intensity at the focus is shown as I_0 (272.11 kWm^{-2}), $L_{eff} = [1 - \exp(-\alpha L)]/\alpha$ is the effective thickness of the sample, and the linear optical absorption coefficient (α) at λ=514 nm is 13.106 m^{-1}. From the experimental CA measurements and the above equations, n_2 was obtained as − 12.9559×10^{-13} m^2/W.

In order to compute the nonlinear absorption coefficient (β) of the Cd(II) complex, OA data are fitted with the eq. (5) to find ΔT [75].

$$T_{OA}(z) = 1 - \frac{\Delta T}{1 + \frac{z^2}{z_0^2}} \tag{5}$$

Based on the open-aperture Z–scan data, the nonlinear absorption coefficient β is calculated by the eq. (6).

$$\beta = \frac{2\sqrt{2}\Delta T}{I_0 L_{eff}} \tag{6}$$

The real and imaginary components of the third-order nonlinear optical susceptibility, $\chi^{(3)}$, are determined by using equations (7) and (8), considering the coefficients n_2 and β.

$$\mathrm{Re}\chi^{(3)}(esu) = \frac{\varepsilon_0 c^2 n_0^2 n_2}{\pi}\left(m^2/W\right) \tag{7}$$

$$\mathrm{Im}\chi^{(3)} = \frac{\varepsilon_0 c^2 n_0 \lambda \beta}{4\pi^2}(m/W) \tag{8}$$

Here, the ε_0, c, and n_0 stand for the permittivity of free space (8.8518×10^{-12} Fm^{-1}), the vacuum speed of light, and the Cd(II) complex's linear refractive index, respectively.

The magnitude of the third-order nonlinear optical susceptibility ($\chi^{(3)}$) and the second-order molecular hyperpolarizability (γ) are calculated using the following equations (9) and (10).

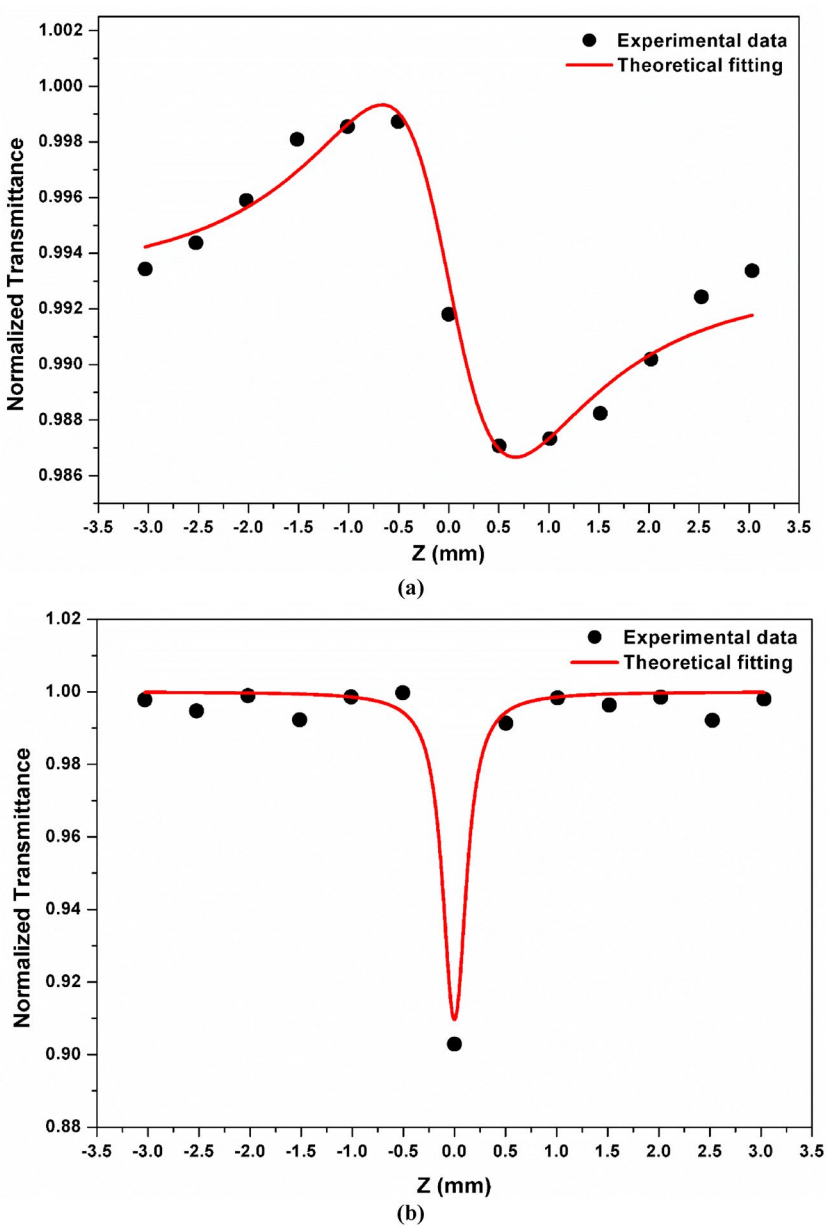

Fig 7 **a** Closed-aperture (CA) Z–scan, **b** Open-aperture (OA) Z–scan data, and their theoretical fitting curves for the Cd(II) complex in ethanol

$$\left|\chi^{(3)}\right| = \sqrt{\left(\mathrm{Re}\chi^{(3)}\right)^2 + \left(\mathrm{Im}\chi^{(3)}\right)^2} \tag{9}$$

$$\mathrm{Re}[\gamma] = \frac{\mathrm{Re}\left[\chi^{(3)}\right]}{Nf^4} \tag{10}$$

Here, N denotes the number of molecules per unit volume, and f represents the local field correction factor $\left(f = \left(n_0^2 + 2\right)/3\right)$ according to the Lorentz expression.

Figure 7a, which shows the pre-focusing peak and post-focusing valley transmittance, corresponds to the negative phase shift resulting from the self-defocusing property of the Cd(II) complex. This peak-valley configuration is a clear indication of negative nonlinear refraction ($n_2 < 0$). Figure 7b displays a minimum (valley) in transmittance at the focal point, indicating the reverse saturable absorption (RSA) behavior of the sample. This RSA behavior reflects the presence of positive nonlinear absorption ($\beta > 0$) in the material. A negative β value corresponds to saturable absorption, while a positive β suggests a two-photon absorption mechanism. Taking into account the results of n_2 and β, the real/imaginary third-order nonlinear optical

Table 6 Open/Closed aperture Z–scan analysis of the Cd(II) complex for NLO parameter determination

Laser beam wavelength (λ)	514 nm
Laser power (P)	28.19 mW
Lens Focal length (f)	200 mm
Optical path difference (Z)	150 mm
Aperture radius (r_a)	1.0 mm
Beam radius of the aperture (ω_a)	1.7 mm
Effective thickness (L_{eff})	9.37 mm
Linear absorption coefficient (α)	13.106 m^{-1}
Nonlinear refractive index (n_2)	-12.9559×10^{-13} m^2 /W
Nonlinear absorption coefficient (β)	107.682×10^{-5} m/W
Real part of third-order nonlinear susceptibility ($Re\chi^{(3)}$)	-92.6246×10^{-4} esu
Imaginary part of third-order nonlinear susceptibility ($Im\chi^{(3)}$)	1874.33×10^{-4} esu
Third-order nonlinear susceptibility ($\chi^{(3)}$)	1876.62×10^{-4} esu
Real part of second-order molecular hyperpolarizability (Re[γ])	-4676.33×10^{-28} esu

susceptibility $\chi^{(3)}$ were obtained at -12.9559×10^{-4} and 107.682×10^{-5} esu, respectively. The obtained third-order nonlinear optical susceptibility ($\chi^{(3)}$) and second-order molecular hyperpolarizability (γ) for the complex are -1876.62×10^{-4} and -4676.33×10^{-28} esu, respectively. Here, the results obtained for the complex were compared with the n_2, β, and $\chi^{(3)}$ values of the KH_2PO_4 (KDP) crystal, known as the NLO material. In the KDP crystal, these parameters change with different wavelengths and laser powers at $n_2 \approx (1–5)\times10^{-16}$ cm^2/W, $\beta \approx \pm(0.1–2)\times10^{-9}$ cm/W, and $|\chi^{(3)}| \approx (0.5–3)\times10^{-13}$ esu values [76–78]. When all the parameters obtained for the Cd(II) complex are compared with these results, it can be shown that the complex can be a candidate for a third-order NLO material.

3.5 The analysis of the refractive index, linear and non-linear optical parameters

The refractive index (n) for the Cd(II) complex in ethanol was acquired by using the following equation [3, 69].

$$n = \frac{1+R}{1-R} + \sqrt{\frac{4R}{(1-R)^2} - k^2} \tag{11}$$

In eq. (11), extinction coefficient ($k = \frac{\alpha\lambda}{4\pi}$), R, α and λ is the reflectance, absorption coefficient, and wavelength, in that sequence. The refractive index values of the Cd(II) complex were obtained at 2.533 and 1.274 at 268 and 214 nm, respectively (see Fig. 8). This n change shows that the complex has an intense absorption band around 214 nm due to the strong absorption effect. In this case, it can be stated that the complex may have the potential to be used in optical sensors or as a UV light-interactive material.

The exploration of nonlinear optical (NLO) molecular systems has garnered considerable interest due to their potential applications in emerging technologies as required by advanced fields like optical signal processing and telecommunications. Organic single crystals have been extensively investigated in the literature due to their remarkable nonlinear optical (NLO) properties, which arise from their high molecular polarizability, extended π-conjugation, and well-ordered crystalline arrangements that facilitate efficient charge transfer and optical nonlinearity [79–82]. In this context, the strategic selection of ligands in coordination complexes has become increasingly important due to the robustness and flexibility of metal–ligand interactions, which facilitate the formation of non-centrosymmetric crystal structures. Such structures are essential for developing materials with second− and third−order NLO features. Moreover, NLO materials with rapid response times and high processability are highly desirable for applications in optoelectronic and photonic technologies. In the current work, the third-order nonlinear optical susceptibility ($\chi^{(3)}$) parameters were investigated by using. Z–scan technique [73, 74] mentioned in the section above. In addition, the $\chi^{(3)}$ parameter within the UV-Vis spectral range (200–600 nm) is computed as a function of the refractive index using eq. (11). Besides, in the UV-Vis range (200–600 nm), the third-order nonlinear susceptibility, $\chi^{(3)}$, is determined as a function of the refractive index by using eq. (12) [83, 84].

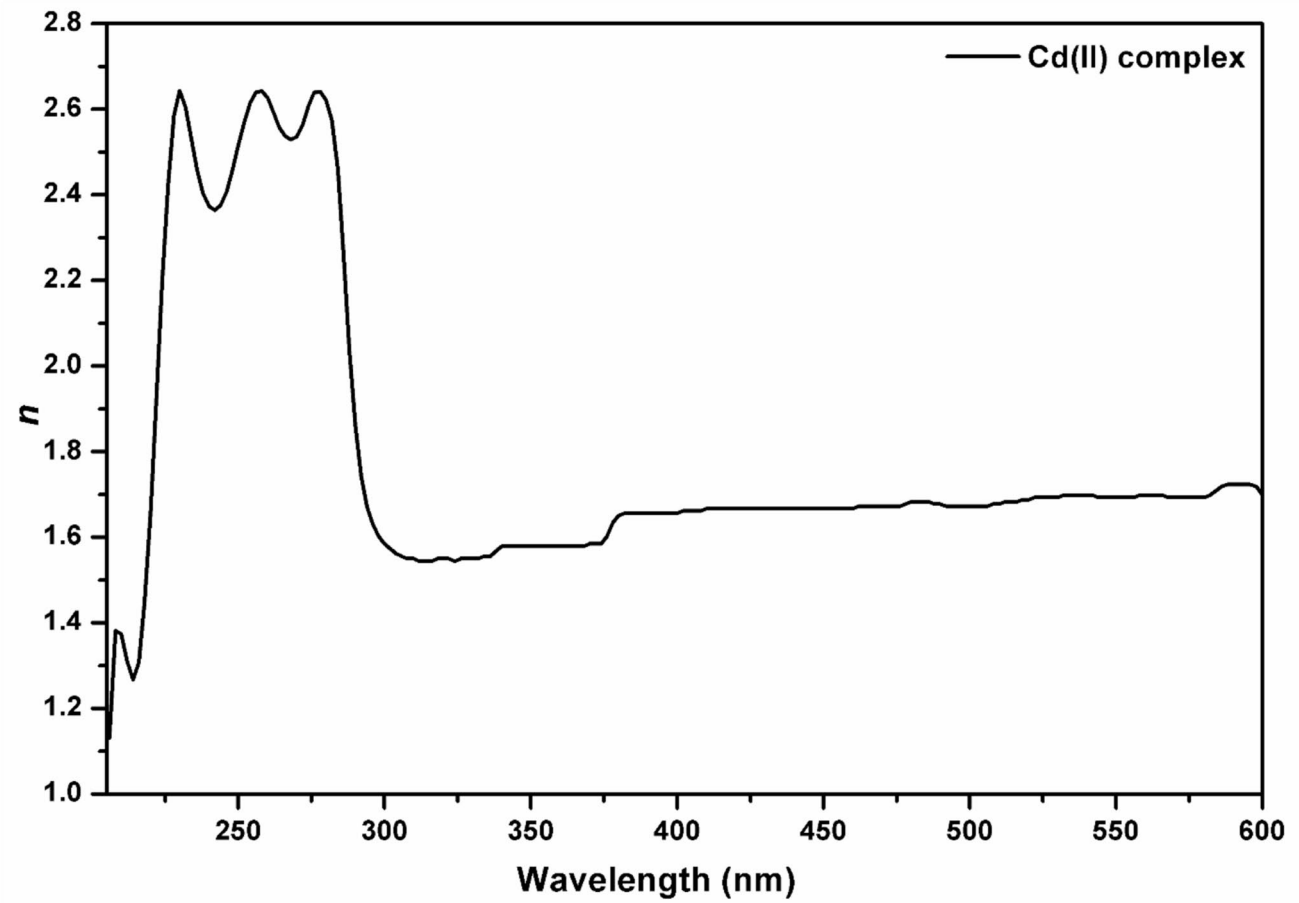

Fig. 8 The refractive index (n) versus wavelength (λ) of the Cd(II) complex

$$\chi^{(3)} = \frac{A}{(4\pi)^4}\left(n^2 - 1\right)^4 \quad (12)$$

In eq. (12), the A parameter is assumed to be approximately 10^{-10} esu for all materials, independent of the frequency. In the UV region, $\chi^{(3)}$ values remain nearly constant up to approximately 4.3 eV, while 51.12×10^{-13}, 51.29×10^{-13} and 51.46×10^{-13} esu were observed at photon energies of 4.7, 4.8 and 5.4 eV (see Fig. 9). From Z–scan CA and OA results, the $\chi^{(3)}$ and γ for Cd(II) complex were found to be 48.0245×10^{-4} and 2424.66×10^{-28} esu, respectively. These results obtained for the Cd(II) complex indicate that the complex is an effective potential candidate for a third-order NLO material.

Using DFT methods at the CAM-B3LYP and HSEh1PBE levels with the LanL2DZ basis set in ethanol, both static and frequency-dependent dynamic properties (at $\lambda = 514$ nm) of the Cd(II) complex were examined, focusing on linear (α and Δα) and nonlinear (β and γ) optical parameters. Table 7 provides a comparative analysis between the obtained results and those of p-nitroaniline (pNA) [85] and urea [86, 87], which are widely considered as reference materials in the field. Furthermore, to achieve a deeper comprehension of the optoelectronic and electronic characteristics of the Cd(II) complex, physical parameters such as polarization (*P*), electric displacement (*D*), electric susceptibility (χ_e), vacuum permittivity (ε_0), relative permittivity (ε_r), and the applied external electric field (*E*) were computed using DFT methods at the CAM-B3LYP and HSEh1PBE levels. The linear, second-order, and third-order optical susceptibility tensors and their corresponding polarization components ($\chi^{(1)}/P^{(1)}$, $\chi^{(2)}/P^{(2)}$, $\chi^{(3)}/P^{(3)}$) were also theoretically evaluated using the same DFT methodologies (see Table 7). As presented in Table 7, the *E*, *P*, and *D* parameters for Cd(II) complex were determined to be $1.614/4.314\times10^{9}$ V/m, $4.042/6.525\times10^{-2}$ C/m^2, and $5.471/2.705\times10^{-2}$ C/m^2, respectively. These findings align well with those

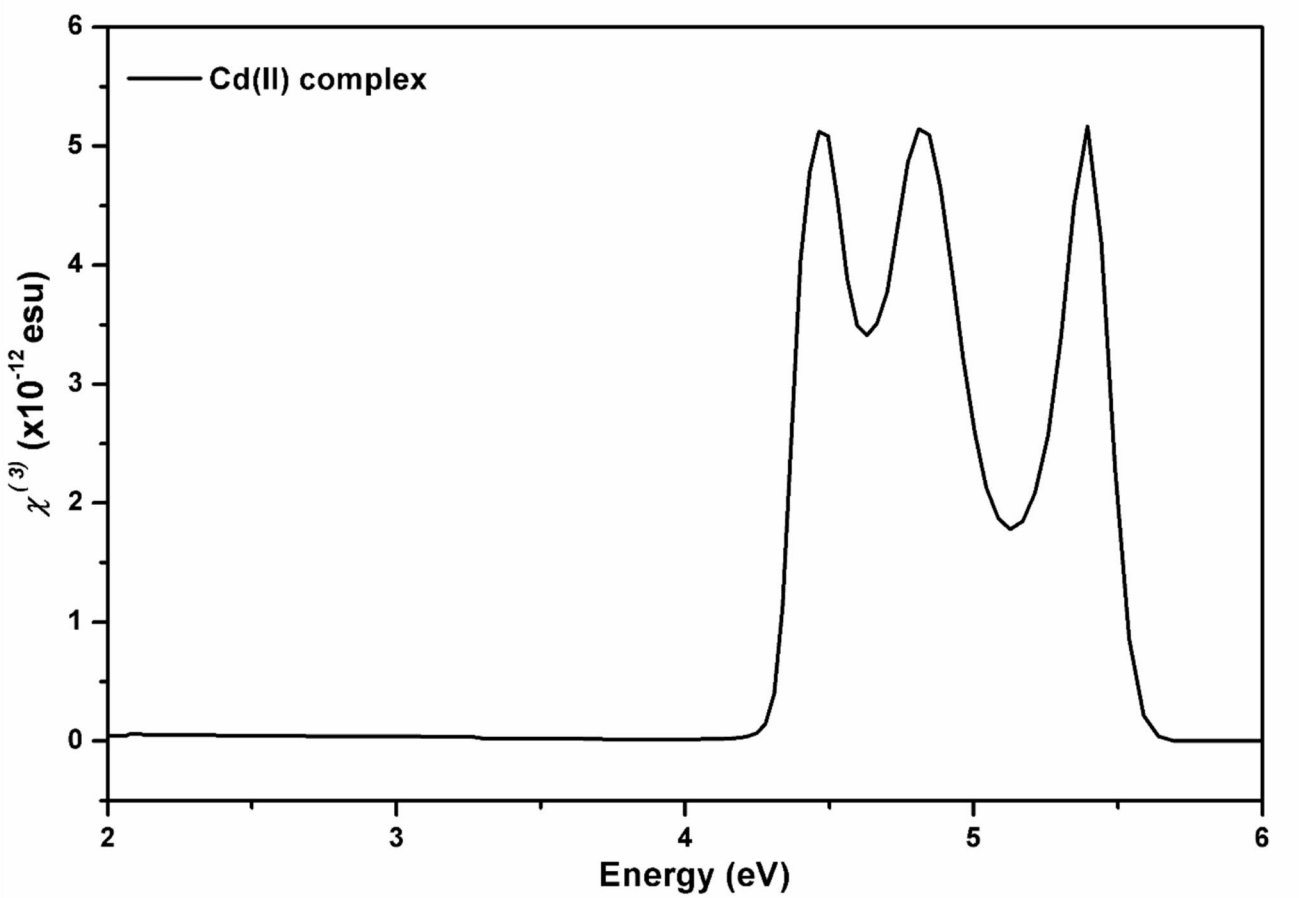

Fig. 9 The third-order nonlinear optical susceptibility $\chi^{(3)}$ of the Cd(II) complex in ethanol

reported for other previously studied metal complexes [88, 89]. From these results, it can be stated that the response of the complex to electric fields is remarkable in optoelectronic and photonic materials research. The static and dynamic linear optical properties, including isotropic and anisotropic polarizabilities (<α(0;0)>/<α(−ω;ω)> and Δα(0;0)/Δα(−ω;ω)), were computed at the same DFT levels. These parameters were determined as 156.65×10^{-24}/62.784×10^{-24} esu and 67.737×10^{-24}/33.437×10^{-24} esu by using CAM-B3LYP level, which are 9.21 and 3.69 times larger than the value of pNA <α(0;0)> pNA (17×10^{-24} esu) [85]. The linear polarizability values determined in this work are notable in comparison to previously reported data for various metal complexes, reflecting the influence of their coordination environments [88, 90].

The static and frequency-dependent dynamic second-order nonlinear optical susceptibility tensor components (<β(0;0,0)>/<β(−ω;ω,0)> relevant to the electro-optic Pockels effect, and <β(−2ω;ω,ω)> corresponding to second harmonic generation (SHG) of the Cd(II) complex were computed at the DFT/CAM-B3LYP level, yielding magnitudes of 869.09×10^{-30}, 340390.4×10^{-30}, and 341.79×10^{-30} esu, respectively (see Table 7). The static β parameter obtained in this study exhibits magnitudes approximately 2715.6 and 6684.6 times greater than those documented for urea (0.32×10^{-30} esu [86] and 0.130×10^{-30} esu [87]), and 94.5 times higher than the value reported for p-nitroaniline (pNA) (9.2×10^{-30} esu [85]). The second-order NLO susceptibility tensor/polarization ($\chi^{(2)}/P^{(2)}$) results obtained with DFT/CAM-B3LYP level, as 30290.45 pm/V / 6986.53×10^{-4} C/m^2, support the β results for the second-order NLO material. Furthermore, the static and frequency-dependent dynamic third-order nonlinear optical (NLO) susceptibility tensor components (<γ(0;0,0,0)>/<γ(−ω;ω,0,0)> corresponding to the quadratic electro-optic Kerr effect, and <γ(−2ω;ω,ω,0)> associated with DC electric-field-induced second harmonic generation (EFISHG) of the Cd(II) complex

Table 7 Average electric field (E), electric polarization (P), electric displacement (D), relative dielectric constant (ε_r), average electric susceptibility (χe), refractive index (n), first-order linear, second-, and third-order nonlinear optical susceptibility ($\chi^{(1)}$, $\chi^{(2)}$ in 10−12 m/V, and $\chi^{(3)}$ in 10−22 m^2/V^2), electric dipole moment (μ, Debye), static- and dynamic-isotropic (<α(0;0)> and <α(−ω;ω)>, × 10−24 esu), and anisotropic polarizability (Δα(0;0) and Δα(−ω;ω), x10−24 esu), static- and dynamic-first- (<β(0;0,0)>, <β(−ω; ω 0)> and <β(−2ω; ω, ω)>, × 10−30 esu) and second-order hyperpolarizabilities (<γ(0;0,0,0)>, <γ(−ω; ω,0,0)> and <γ(−2 ω; ω, ω,0)>, × 10−36 esu) for the Cd(II) complex

Parameter	CAM-B3LYP/LanL2DZ	HSEh1PBE/LanL2DZ
E (×10^9 V/m)	1.614	4.314
P (×10^{-2} C/m^2)	4.042	6.525
D (×10^{-2} C/m^2)	5.471	2.705
ε_r	3.828	1.708
χ_e	2.828	0.708
n	1.956	1.307
$\chi^{(1)}$	2.828	0.708
$P^{(1)}$ (×10^{-2} C/m^2)	4.041	2.705
$\chi^{(2)}$	30290.45	94.10
$P^{(2)}$ (×10^{-4} C/m^2)	6986.53	155.06
$\chi^{(3)}$	57768.9	− 1720.1
$P^{(3)}$ (×10^{-4} C/m^2)	2150.57	− 1222.8
μ	8.434	5.099
μ	6.20 (pNA) [85] and 4.56 (Urea) [86]	
<α(0;0)>	156.65	252.02
<α(−ω;ω)>	62.784	35.438
<α>	17 (pNA) [85]	
Δα (0;0)	67.737	164.71
Δα (−ω;ω)	33.437	30.848
<β(0;0,0)>	869.09	282.89
<β(−ω;ω,0)>	340390.4	892.36
<β(−2ω;ω,ω)>	341.79	800.45
<β>	9.2 (pNA) [85] and 0.32 (Urea) [86] and 0.13 (Urea) [87]	
<γ(0;0,0,0)>	3407.19	− 46406.5
<γ(−ω;ω,0,0)>	− 1974417.9	− 280197.8
<γ(−2ω;ω,ω,0)>	− 15182.76	41894.86
<γ>	15.0 (pNA) [85] and 7 (Urea) [86]	

were calculated at the DFT/CAM-B3LYP level, yielding values of 3407.19×10^{-36}, -1974417.9×10^{-36} and − 15182.76×10^{-36} esu, respectively. At the CAM-B3LYP level of theory, the <γ(0;0,0,0)> value (3407.19×10^{-36}) was found to be 227.1-fold and 486.7-fold greater than the reported values for p-nitroaniline (pNA) (15×10^{-36} esu) [85] and urea (7×10^{-36} esu) [86], respectively. As seen from Table 7, the second-order nonlinear optical susceptibility tensors and corresponding polarization parameters ($\chi^{(3)}/P^{(3)}$) associated with the γ values were computed at the DFT/CAM-B3LYP level, yielding magnitudes of 57768.9×10^{-22} m^2/V^2 and 2150.57×10^{-4} C/m^2, respectively. According to the evaluated $\chi^{(2)}/\beta$ and $\chi^{(3)}/\gamma$ parameters, the Cd(II) complex demonstrates significant enhancement in both second- and third-order nonlinear optical properties. Exhibiting significant frequency dispersion with a high refractive index, a strong ICT dipole, and pronounced third-order NLO susceptibility ($\chi^{(3)}$), the Cd(II) complex exhibits potential applications in photonic devices. In particular, its ability to suppress or modulate transmission under high optical power makes it suitable for intensity-dependent detectors. Its large Kerr-type nonlinearity also allows for efficient phase shifting of optical signals, making it a promising candidate for phase-modulated sensors.

The facilitation of intramolecular charge transfer (ICT) by a decreased HOMO–LUMO energy gap (ΔE) plays a pivotal role in enhancing nonlinear optical (NLO) responses. Notably, the CAM-B3LYP functional, which confers a low ΔE that favors charge transfer interactions, also provides high first- and second-order hyperpolarizability. This trend underlines the established correlation between minimized energy gaps and improved NLO behavior (see Tables S2 and 7).

The third-order nonlinear optical parameters of the synthesized metal complexes reveal distinct

Table 8 The comparison of third-order nonlinear optical parameters of Cd(II) complex and other materials

Materials	n_2 [m^2/W]	Re$\chi^{(3)}$ [esu]	β [m/W]	Im$\chi^{(3)}$ [esu]	$\lvert\chi^{(3)}\rvert$ [esu]	References
Cd(II) complex	-12.9559×10^{-13}	-92.6246×10^{-4}	107.682×10^{-5}	1874.33×10^{-4}	1876.62×10^{-4}	Present work
Zn(II) complex	-1.35×0^{-11}	-6.34×10^{-6}	2.63×10^{-6}	0.512×10^{-7}	6.36×10^{-6}	[93]
[ADI (3-AP) Cd]	2.48505×10^{-11}	1.59434×10^{-9}	1.0041×10^{-4}	3.24564×10^{-8}	3.24955×10^{-8}	[94]
Cu(II) complex	-88.69×10^{-10}	-4.65×10^{-3}	748×10^{-5}	0.55×10^{-3}	4.68×10^{-3}	[92]
CdS/NBS glass	-2.16×10^{-16}	-1.20×10^{-10}	6.32×10^{-11}	2.14×10^{-12}	1.20×10^{-10}	[91]
Co/Cu metal complexes	$\sim5.64143\times10^{-20}$		$\sim1.43905\times10^{-13}$		$\sim3.0037\times10^{-13}$	[95]
KH_2PO_4 (KDP)	$(1–5)\times10^{-20}$		$\pm(0.1–2)\times10^{-11}$		$(0.5–3)\times10^{-13}$	[76–78]

behaviors depending on the nature of the central ion (see Table 8). The Cd(II) complex exhibited a high third-order susceptibility ($|\chi^{(3)}| \approx 1.88\times10^{-11}$ esu), which is several orders of magnitude greater than conventional reference materials such as KDP crystals (10^{-13} esu range [76–78]) and CdS/NBS glass ($\sim10^{-10}$ esu [91]). This enhanced response can be attributed to the strong electronic delocalization within the Cd(II) coordination environment, facilitating efficient charge transfer and polarization under optical excitation. In addition, the negative nonlinear refractive index ($n_2 = -1.29\times10^{-12}$ m^2/W) together with a significant two-photon absorption coefficient ($\beta = 1.08\times10^{-3}$ m/W) indicates a self-defocusing effect dominated by nonlinear absorption, suggesting the potential of this complex for optical limiting applications. The Cu(II) complex, on the other hand, displayed an exceptionally large susceptibility ($|\chi^{(3)}| \approx 4.68\times10^{-3}$ esu [92]), surpassing most reported molecular and inorganic systems. While this highlights its promise for high-performance photonic devices such as all-optical switches, the accompanying large β value reflects strong nonlinear absorption losses that could limit its practical efficiency unless carefully optimized. In contrast, the Zn(II) complex showed a considerably weaker nonlinear response ($|\chi^{(3)}| \approx 6.36\times10^{-6}$ esu [93]), consistent with its less pronounced charge transfer interactions, and thus may be considered as a reference point rather than a candidate for nonlinear applications. As a whole, these findings demonstrate that metal coordination strongly influences the magnitude and nature of nonlinear optical responses, with Cd(II) and Cu(II) complexes emerging as promising systems for third-order NLO applications.

The effects of metal ions and coordination environment on the structure are clearly seen with the changes in the calculated NLO values. These effects can sometimes be interpreted directly or indirectly with other molecular reactivity parameters (such as hardness, electrophilicity, and nucleophilicity index). While the Cd complex shows low hardness and nucleophilicity results, it displays high electrophilicity values. Functional groups including −Cl, −Br, $-CH_3$, and $-OCH_3$ have been demonstrated to enhance second harmonic generation (SHG) efficiency in certain molecular frameworks by acting as potent electron donors [93, 96, 97]. It can be said that the Cl atom and coordination environment at the 6-position of the 6-ClPCA ligand used in the Cd(II) complex have an enhancing effect on the NLO parameters.

In conclusion, the findings derived from both experimental and theoretical approaches in this work are anticipated to inform and support future investigations, as well as the design and fabrication of next-generation optoelectronic materials and devices. The Cd(II) complex, which shows effective NLO properties, has a high potential to be a suitable material for NLO optical devices, as third-order NLO results measured by Z–scan and calculated second- and third-order NLO parameters.

3.6 The analysis of the α-glucosidase inhibition assay and molecular docking

The IC_{50} values of various metal complexes and reference compounds were evaluated to assess their comparative bioactivity (see Table 9). Among the tested compounds, 6-chloropicolinic acid (6-ClpicH) was found to be inactive, while its cadmium (II) complex, $[Cd(6\text{-ClPCA})_2]_n$, exhibited moderate inhibitory activity with an IC_{50} of 383.71 ± 1.54 μM. Incorporation of 6-methylpicolinic acid (6-mpa) as a ligand generally enhanced biological activity. For instance, the cadmium-based complex $[Cd(NCS)(6\text{-mpa})]_n$ showed improved activity ($IC_{50} = 240.08 \pm 1.21$ μM [21]), while $Cd(6\text{-mpa})_2(4(5)MeI)_2$ demonstrated comparable

Table 9 In vitro inhibition IC50 values (μM) of the Cd(II) complex for α–glucosidase, characterization of protein–ligand interactions and calculated distances based on docking data

Compound	IC_{50} (μM)[a]	Substrate	Receptor	Interaction	Distance (Å)	K_i (μM)	Binding energy (kcal/mol)
6−Chloropicolinic acid (6-ClpicH)	not active	C=O (O)	TRY-566 (O)	Conventional H-Bond	2.52	21.34	− 6.37
$[Cd(6\text{-}ClPCA)_2]_n$	383.71 ± 1.54	6-ClPCA (Cl)	GLUE-497 (OE2)	Charge-Charge	3.80		
$[Cd(NCS)(6\text{-}mpa)]_n$ [b]	240.08 ± 1.21	6-ClPCA (C)	GLU-497 (OE2)	Charge-Charge	4.71		
$Cd(6\text{-}mpa)_2(4(5)MeI)_2$ [c]	260.20 ± 1.50	6-ClPCA (C)	GLU-497 (OE2)	Charge-Charge	4.78		
$Cd(6\text{-}mpa)_2(dmdpy)$ [d]	>600	6-ClPCA (C)	GLU-497 (OE2)	Charge-Charge	5.53		
$[Cd(6\text{-}mpa)_2(H_2O)_2]\cdot 2H_2O$ [e]	4.966 ± 1.02	6-ClPCA (C)	GLU-497 (OE1)	Charge-Charge	4.97		
$Zn(6\text{-}mpa)_2(H_2O)]\cdot 2H_2O$ [e]	460 ± 0.001	6-ClPCA (C)	GLU-497 (OE1)	Charge-Charge	5.04		
$[Zn(6\text{-}Clpic)(pic)(H_2O)_2]$ [f]	440 ± 0.002	6-ClPCA (C)	GLU-497 (OE1)	Charge-Charge	4.66		
Genistein	13.56±1.21	6-ClPCA (N)	GLU-570 (OE2)	Charge-Charge	5.54		
		6-ClPCA (C)	GLU-570 (OE2)	Charge-Charge	4.64		
		6-ClPCA (C)	GLU-570 (OE2)	Charge-Charge	5.30		
		6-ClPCA (C)	GLU-570 (OE2)	Charge-Charge	3.61		
		6-ClPCA (C)	GLU-570 (OE2)	Charge-Charge	3.77		
		6-ClPCA (C)	GLU-570 (OE2)	Charge-Charge	4.88		
		6-ClPCA	PRO-567 (C)	Pi-Sigma	3.54		
		6-ClPCA	LYS-568	Pi-Alkyl	4.31		
		6-ClPCA	LYS-569	Pi-Alkyl	4.77		

[a]IC_{50} values represent the means ± S.E.M. of three parallel measurements ($p < 0.05$)

[b]From reference [21]

[c]From reference [22]

[d]From reference [23]

[e]From reference [26]

[f]From reference [3]

activity (IC_{50} = 260.20 ± 1.50 μM [22]). Notably, the complex $[Cd(6\text{-}mpa)_2(H_2O)_2]\cdot 2H_2O$ exhibited the highest potency among all tested compounds, with a significantly lower IC_{50} value of 4.966 ± 1.02 μM [26], indicating a strong structure–activity relationship possibly influenced by the coordination of water molecules. In contrast, $Cd(6\text{-}mpa)_2(dmdpy)$ was largely inactive (IC_{50} > 600 μM [23]), suggesting that the nature of the co-ligand critically affects biological response. It can be inferred that both the coordination environment and the metal ions have a slight influence on α-glucosidase inhibitory activity. On the other hand, synthesized previously in our study, zinc-based analogues, including $[Zn(6\text{-}mpa)_2(H_2O)]\cdot 2H_2O$ and $[Zn(6\text{-}Clpic)(pic)(H_2O)_2]$, showed relatively weak activity with IC_{50} values of 460 ± 0.001 μM and 440 ± 0.002 μM, respectively. Genistein, as the reference compound, exhibited potent inhibitory activity with an IC_{50} of 13.56 ± 1.21 μM. A notable change in α-glucosidase inhibitory activity was observed upon replacing Cd(II)/6-ClPCA with Zn(II)/6-mpa or pic ligands. The coordination geometry around the metal center was determined to have a negligible effect on α-glucosidase inhibitory activity. To summarize, the results indicate that cadmium(II) coordination complexes, particularly those containing 6-mpa and coordinated water

molecules, exhibit promising inhibitory activity and are worthy of further investigation as potential bioactive agents.

The AutoDock4 program [55] was utilized to investigate the molecular interactions at the binding site between the Cd(II) complex and the target protein, using the template structure of S. *cerevisiae*

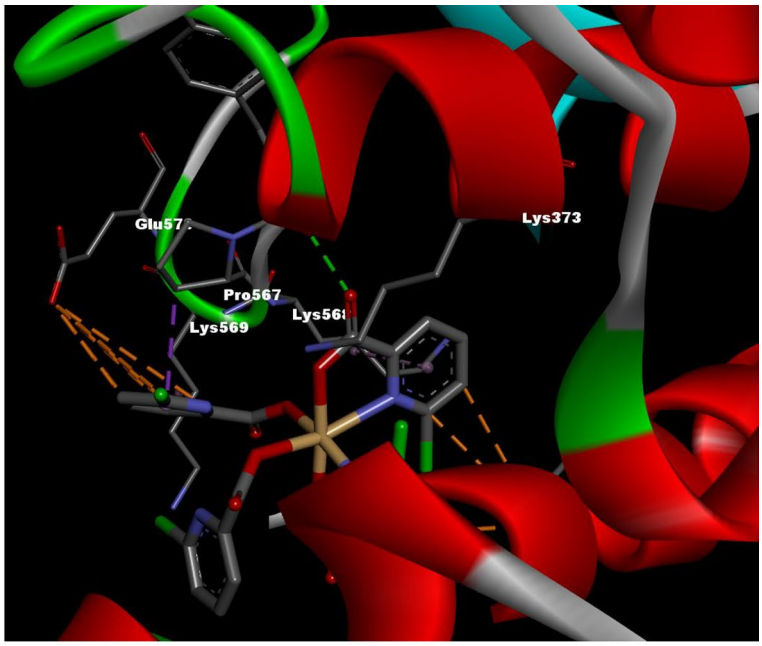

(a)

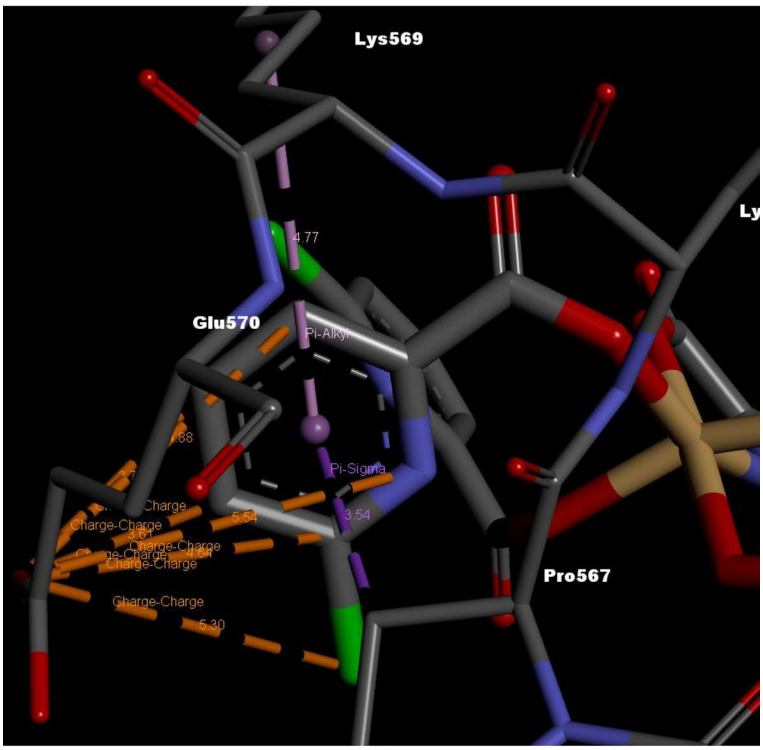

(b)

Fig 10 **a** 3D interaction maps **b** left side of 3D interaction maps **c** right side of 3D interaction maps and **d** 2D interaction maps illustrating the contacts between protein residues and the ligand of the Cd(II) complex

Fig 10 continued

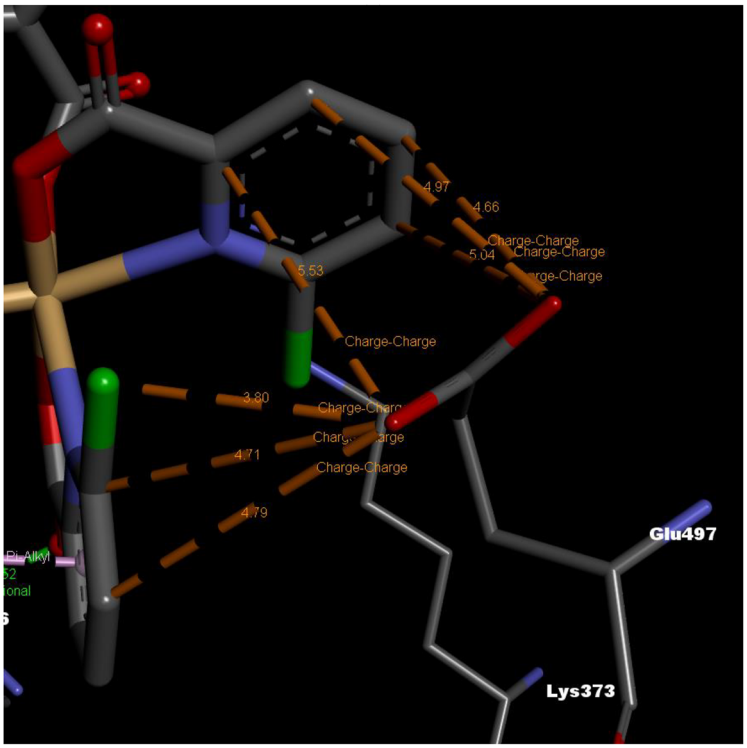

(c)

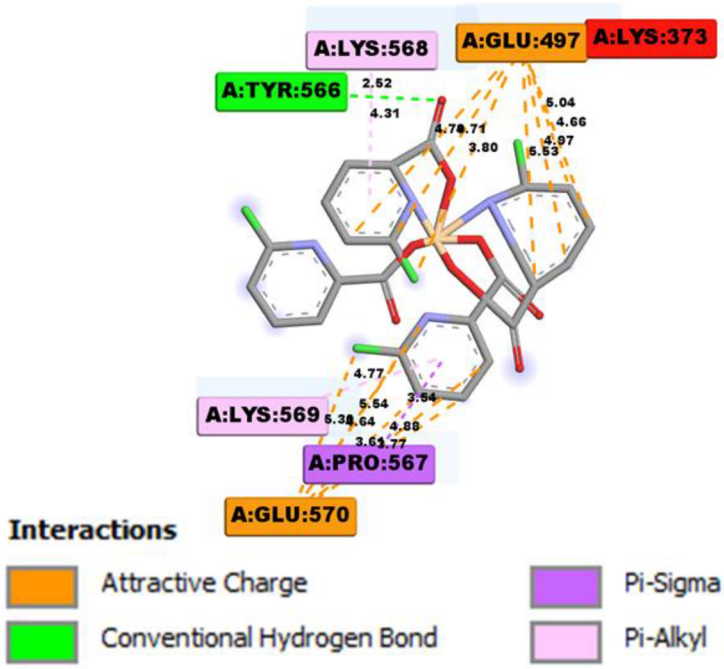

(d)

isomaltase (PDBID: 3A4A). The docking results determined both the binding energies and the estimated inhibition constants (K_i), as can be seen in Table 9. Discovery Studio 4.0 [59] was employed to visualize the 2D and 3D interactions between the ligands and amino acid residues (see Fig. 10).

The binding energy values for genistein, used as the standard inhibitor [58], and Cd(II) complex were determined to be -6.35 and -6.37, kcal/mol. The corresponding inhibition constant (K_i) values were calculated at 22.06 and 21.34 μM, respectively (see Tables 8 and S3). The interactions of certain parts of the Cd(II) complex with amino acid residues are presented in Table 9 and Fig. 10. These interactions include conventional hydrogen bond, pi-sigma, pi-alkyl, and charge-charge interactions. Based on the docking results of the complex, the interaction distances ranging from 2.52 to 5.54 Å were observed in the conventional hydrogen bond/pi-cation interactions between 6-ClPCA (C=O)/ 6-ClPCA-(Cl), (C), (N) and the amino acid residues Try566(O)/Glu497(OE2), Glu497(OE1), and Glu570(OE2) for Cd(II) complex (Table 9). Additionally, the notable interactions, including pi-sigma and pi-alkyl calculated at distances ranging from 3.54 to 4.77 Å, were observed between 6-ClPCA and the amino acid residues Pro567(C) for pi-sigma, and Lys568/Lys569 for pi-alkyl. Compared to these genistein results [58], the conventional hydrogen bond and pi-alkyl interactions observed at distances of 2.73/2.45/3.29/2.88/3.14 and 4.19/5.25 Å are noteworthy. These interactions occur between the C=O (benzopyran-4-one)/CO (5-hydroxy-benzopyran-4-one)/CO (7-hydroxy-benzopyran-4-one) and phenyl ring, and the Ile272/Ser298/Leu297/Ser291/Ala292 and Arg263/Ile272 residues, as shown in Table S3.

The 1,4-glycosidic bond in polysaccharides is hydrolyzed by α-glucosidase, leading to the production of α-D-glucose. Consequently, during absorption, α-D-glucose is released into the bloodstream, contributing to postprandial hyperglycemia [98, 99]. α-Glucosidase consists of residues such as Asp, Glu, Gly, His, Phe, Thr, Tyr, Leu, Lys, etc. Moreover, residues like Arg, Asp, Glu, Trp, and Tyr are particularly located at the entrance of the active site of α-glucosidase and are crucial for the enzyme's catalytic activity [100–102]. Table 9 and Fig. 10 show that the synthesized complex interacted with some of these residues through conventional hydrogen bonding, pi-sigma, pi-alkyl, and charge-charge interactions. These interactions with the active site of α-glucosidase are thought to block substrate entry, reduce catalytic activity, and ultimately inhibit α-glucosidase function. Additionally, the hydrogen bond interactions may reduce the hydrophilicity of α-glucosidase and increase its hydrophobicity, thereby enhancing the stability of the inhibitor-enzyme complex. Moreover, considering the enzyme kinetic studies [103–105], the majority of metal complexes are non-competitive α-glucosidase inhibitors, and the Cd(II) complex we synthesized is predicted to be a non-competitive inhibitor as well.

The IC_{50} values of the Hg(II) and Cu(II) complexes against α-glucosidase were determined to be 0.184 ± 0.015 μM and 1.685 ± 0.020 μM, respectively, whereas their IC_{50} values in cytotoxicity assays on a healthy cell line were found to be 24.141 ± 1.039 μM and 53.435 ± 1.120 μM in our previous reports [24, 106]. These findings indicate that the inhibitory concentrations are approximately 131.20-fold and 31.71-fold lower than the concentrations required to induce cytotoxic effects. Thus, the cytotoxic impact of the Hg and Cu complexes on normal cells can be regarded as negligible. Consequently, despite the well-documented toxicity of mercury as a heavy metal, when incorporated into stable complex structures, its detrimental effects on living cells appear minimal, supporting its potential application as an α-glucosidase inhibitor. It is noteworthy that although free metal ions can exhibit significant toxicity at elevated concentrations, metal complexes offer several advantages, including strong and selective interactions with enzyme active sites and the ability to modulate enzyme conformation through binding to residues located near the catalytic center [103, 107]. Considering the moderate inhibition value of the Cd(II) complex in this study and the above results, the cytotoxicity study was not taken into consideration.

4 Conclusions

In this study, a novel metal complex, {[Cd(6-ClPCA)$_2$]$_n$}, was successfully synthesized in crystalline form and subjected to comprehensive characterization using both experimental and theoretical techniques. The molecular structure was confirmed via single-crystal X-ray diffraction. At the same time, vibrational and electronic properties were supported by FT-IR and UV-Vis spectroscopy in conjunction with DFT calculations using different functionals. When the structural and vibration parameters of the selected DFT methods were evaluated in terms of their compatibility with the experimental results, the B3PW91 method gave the best results in terms of bond lengths. In contrast, the HSEh1PBE and ωB97XD methods provided the best agreement in bond angle parameters. It was found that the performance of B3LYP in predicting vibrational frequencies

is inferior to that of other functionals, whereas HSEh1PBE provides more accurate results. The experimental refractive index and band gap derived from the UV-Vis spectroscopic data in ethanol were examined. Furthermore, the Z−scan technique was used to investigate the nonlinear optical refractive index/absorption coefficient (n_2/β), the real and imaginary third-order nonlinear optical susceptibility ($\chi^{(3)}$), and second-order molecular hyperpolarizability (γ) for the Cd(II) complex. The α-glucosidase inhibition assay and molecular docking study were also performed. The IC_{50} value of Cd(II) complex against α-glucosidase was found to be 383.71 μM. From the Z−scan data, the $Re\chi^{(3)}$ and $Im\chi^{(3)}$ parameters were obtained at − 92.6246×10^{-4} and 1874.33×10^{-4} esu. The total $\chi^{(3)}$ and γ for the Cd(II) complex found to be 1876.62×10^{-4} and − 4676.33×10^{-28} esu, respectively. At the DFT/CAM-B3LYP level, the obtained results of the $\chi^{(2)}$ (30290.45 pm/V)/β (869.09×10^{-30}, 340390.4×10^{-30}, and 341.79×10^{-30} esu) and $\chi^{(3)}$ (57768.9×10^{-22} m^2/V^2)/γ (3407.19×10^{-36}, − 1974417.9×10^{-36} and − 15182.76×10^{-36} esu) demonstrate the Cd(II) complex was remarkable for the second− and third−order NLO features. Compared with previous similar structures, it was observed that ligand and metal ion exchange significantly affected the NLO and α-glucosidase inhibitory activity. In comparison to previously published works, the present study makes a multidimensional contribution by integrating crystallographic, spectroscopic, theoretical, optical, and biological assessments within a single framework. The comprehensive approach addresses key gaps in the current literature, where such properties are often explored in isolation. This work delivers an in-depth comparative analysis of calculated and experimentally observed structural, spectral, and optical features of the Cd(II) complex. The NLO and *in vitro* findings provide significant guidance for the rational design and synthesis of novel picolinate-based metal complexes. As a result, the findings not only enrich the fundamental understanding of metal-based complexes but also highlight the potential of the title compound for future development in both optoelectronic and pharmaceutical applications.

Author contributions

Davut Avcı: Methodology, Software, Data curation, Formal analysis, Writing—original draft, Writing-review&editing. Fatih Sönmez: Formal analysis, Investigation. Adil Başoğlu: Investigation, Methodology. Ömer Tamer: Investigation, Software. Yusuf Atalay: Methodology, Software. Necmi Dege: Data curation, Formal analysis, Visualization. Belma Zengin Kurt: Formal analysis.

Funding

The authors have not disclosed any funding.

Data availability

Datasets generated during the current study are available from the corresponding author on reasonable request.

Declarations

Competing interests The authors have no conflicts of interest to declare that are relevant to the content of this article.

Ethical approval No funding was received to assist with the preparation of this manuscript.

Supplementary Information The online version contains supplementary material available at https://doi.org/10.1007/s10854-025-16136-5.

References

1. N. Dege, Ö. Tamer, M. Şimşek, D. Avcı, M. Yaman, A. Başoğlu, Y. Atalay, Experimental and theoretical approaches on structural, spectroscopic (FT-IR and UV-Vis), nonlinear optical, and molecular docking analyses for Zn (II) and Cu(II) complexes of 6-chloropyridine-2-carboxylic acid. Appl. Organomet. Chem. **36**, e6678 (2022)
2. M. Şimşek, Ö. Tamer, N. Dege, D. Avcı, Y. Atalay, Investigation on the effect of complex formation on prominent high static/dynamic first and second hyperpolarizability of Co(II) complex including 4-chloro-Pyridine-2-Carboxylic acid. Mater. Sci. Semicond. Process. **188**, 109179 (2025)

3. N. Dege, Ö. Özge, D. Avcı, A. Başoğlu, F. Sönmez, M. Yaman, Ö. Tamer, Y. Atalay, B.Z. Kurt, Concentration effects on optical properties, DFT, crystal characterization and α-glucosidase activity studies: novel Zn(II) complex. Spectrochim. Acta A Mol. Biomol. Spectrosc. **262**, 120072 (2021)
4. N. Dege, Ö. Tamer, M. Yaman, A. Başoğlu, D. Avcı, Y. Atalay, Crystallographic, spectroscopic, thermal, optical investigations and density functional theory calculations for novel Co(II) and Mn(II) complexes. Appl. Phys. A **127**, 132 (2021)
5. D. Avcı, H.E. Cömert, F. Sönmez, N. Dege, Ö. Tamer, Y. Atalay, Comparative assessment of structure–property relationships of new Cu(II) complex in selected density functionals. Spectrochim. Acta. A Mol. Biomol. Spectrosc. **305**, 123489 (2024)
6. S. Zinatloo-Ajabshir, M. Salavati-Niasari, Preparation of magnetically retrievable $CoFe_2O_4$@SiO_2@$Dy_2Ce_2O_7$ nanocomposites as novel photocatalyst for highly efficient degradation of organic contaminants. Compos. Part B Eng. **174**, 106930 (2019)
7. S. Zinatloo-Ajabshir, M.S. Morassaei, M. Salavati-Niasari, Eco-friendly synthesis of $Nd_2Sn_2O_7$–based nanostructure materials using grape juice as green fuel as photocatalyst for the degradation of erythrosine. Compos. Part B Eng. **167**, 643–653 (2019). https://doi.org/10.1016/j.compositesb.2019.03.045
8. A. Yousefi, S. Zinatloo-Ajabshir, M. Jekle, M.Y. Panah, Rapid and green combustion synthesis of dysprosium cerium oxide nanostructures: incorporation into wheat starch/sage seed gum hybrid composites. Int. J. Biol. Macromol. **308**, 142502 (2025)
9. M. Amiri, S. Zinatloo-Ajabshir, M. Ahmadi-Zeidabadi, F. Sharifianjazi, Innovative ultrasound assisted synthesis of sponge like cerium dioxide nanostructure using *Rosa Damascena* extract and its efficient performance for cancer therapy. Sci. Rep. **15**, 933 (2025)
10. S. Zinatloo-Ajabshir, S. Rakhshani, Z. Mehrabadi, M. Farsadrooh, M. Feizi-Dehnayebi, S. Rakhshani, M. Dušek, V. Eigner, S. Rtimi, T.M. Aminabhavi, Novel rod-like $[Cu(phen)_2(OAc)]\cdot PF_6$ complex for high-performance visible-light-driven photocatalytic degradation of hazardous organic dyes: DFT approach, Hirshfeld and fingerprint plot analysis. J. Environ. Eng. Manage. **350**, 119545 (2024)
11. S. Zinatloo-Ajabshir, M. Emsaki, G. Hosseinzadeh, Innovative construction of a novel lanthanide cerate nanostructured photocatalyst for efficient treatment of contaminated water under sunlight. J. Colloid Interface Sci. **619**, 1–13 (2022)
12. S. Moshtaghi, S. Zinatloo-Ajabshir, M. Salavati-Niasari, Nanocrystalline barium stannate: facile morphology-controlled preparation, characterization and investigation of optical and photocatalytic properties. J. Mater. Sci. Mater. Electron. **27**, 834–842 (2016)
13. S. Zinatloo-Ajabshir, M. Salavati-Niasari, Preparation and characterization of nanocrystalline praseodymium oxide via a simple precipitation approach. J. Mater. Sci. Mater. Electron. **26**, 5812–5821 (2015)
14. S. Moshtaghi, S. Zinatloo-Ajabshir, M. Salavati-Niasari, Preparation and characterization of BaSnO3 nanostructures via a new simple surfactant-free route. J. Mater. Sci. Mater. Electron. **27**, 425–435 (2016)
15. S. Zinatloo-Ajabshir, M.S. Morassaei, O. Amiri, M. Salavati-Niasari, L.K. Foong, $Nd_2Sn_2O_7$ nanostructures: green synthesis and characterization using date palm extract, a potential electrochemical hydrogen storage material. Ceram. Int. **46**(11), 17186–17196 (2020). https://doi.org/10.1016/j.ceramint.2020.03.014
16. Y. Zhang, X. Xu, Machine learning band gaps of Doped-TiO_2 photocatalysts from structural and morphological parameters. ACS Omega **5**, 15344–15352 (2020)
17. Y. Zhang, X. Xu et al., Machine learning optical band gaps of doped-ZnO films. Optik **217**, 164808 (2020)
18. S. Anand, S.D.K.R. Pai, A. Kumar, C.V. Yelamaggad, Affordable two-dimensional layered Cd(II) coordination polymer: high-performance pseudocapacitor electrode behavior. ACS Omega **9**(40), 41807–41818 (2024)
19. T.S. Munonde, P.N. Nomngongo, Nanocomposites for electrochemical sensors and their applications on the detection of trace metals in environmental water samples. Sensors **21**, 131 (2021)
20. M. Sohrabi, M.R. Binaeizadeh, A. Iraji, B. Larijani, M. Saeedi, M. Mahdavi, A review on a-glucosidase inhibitory activity of first row transition metal complexes: a futuristic strategy for treatment of type 2 diabetes. RSC Adv. **12**, 12011–12052 (2022)
21. D. Avcı, S. Altürk, F. Sönmez, Ö. Tamer, A. Başoğlu, Y. Atalay, B.Z. Kurt, N. Dege, Three novel Cu(II), Cd(II) and Cr(III) complexes of 6-Methylpyridine-2-carboxylic acid with thiocyanate: synthesis, crystal structures, DFT calculations, molecular docking and α-Glucosidase inhibition studies. Tetrahedron **74**, 7198–7208 (2018)
22. D. Avcı, S. Altürk, F. Sönmez, Ö. Tamer, A. Başoğlu, Y. Atalay, B.Z. Kurt, N. Dege, A novel series of M(II) complexes of 6-methylpyridine-2-carboxylic acid with 4(5) methylimidazole: synthesis, crystal structures, α-glucosidase activity, density functional theory calculations and molecular docking. Appl. Organometal. Chem. **33**, e4935 (2019)
23. D. Avcı, S. Altürk, F. Sönmez, Ö. Tamer, A. Başoğlu, Y. Atalay, B.Z. Kurt, Synthesis, DFT calculations and molecular docking study of mixed ligand metal complexes containing 4,4′-dimethyl-2,2′-bipyridyl as α-glucosidase inhibitors. J. Mol. Struct. **1205**, 127655 (2020)
24. D. Avcı, S. Altürk, F. Sönmez, Ö. Tamer, A. Başoğlu, Y. Atalay, B.Z. Kurt, N. Dege, A novel series of mixed-ligand M(II) complexes containing 2,2′-bipyridyl as potent α-glucosidase inhibitor: synthesis, crystal structure, DFT calculations, and molecular docking. JBIC J. Biol. Inorg. Chem. **24**, 747–764 (2019)
25. D. Avcı, S. Altürk, F. Sönmez, Ö. Tamer, A. Başoğlu, Y. Atalay, B.Z. Kurt, N. Dege, Novel Cu(II), Co(II) and Zn(II) metal complexes with mixed-ligand: synthesis, crystal structure, α-glucosidase inhibition, DFT calculations, and molecular docking. J. Mol. Struct. **1197**, 645–655 (2019)
26. D. Avcı, S. Altürk, F. Sönmez, Ö. Tamer, A. Başoğlu, Y. Atalay, B.Z. Kurt, N. Dege, Novel metal complexes containing 6-methylpyridine-2-carboxylic acid as potent α-glucosidase inhibitor: synthesis, crystal structures, DFT calculations, and molecular docking. Mol. Divers. **25**(1), 171–189 (2020). https://doi.org/10.1007/s11030-020-10037-x
27. Y. Yoshikawa, R. Hirata, H. Yasui, H. Sakurai, Alpha−glucosidase inhibitory effect of anti−diabetic metal ions and their complexes. Biochimie **91**, 1339–1341 (2009)
28. E. Ueda, Y. Yoshikawa, H. Sakurai, Y. Kojima, N.M. Kajiwara, In vitro α-glucosidase inhibitory effect of Zn(II) complex with 6-methyl-2-picolinmethylamide. Chem. Pharm. Bull. **53**(4), 451–452 (2005)
29. Y. Yoshikawa, E. Ueda, K. Kawabe, H. Miyake, T. Takino, H. Sakurai, Y. Kojima, Development of new insulinomimetic zinc(II) picolinate complexes with a $Zn(N_2O_2)$ coordination mode: structure characterization, in vitro, and in vivo studies. J. Biol. Inorg. Chem. **7**, 68–73 (2002)
30. D. Avcı, Ö. Özge, F. Sönmez, Ö. Tamer, A. Başoğlu, Y. Atalay, B.Z. Kurt, *In vitro* α-glucosidase, docking and density functional theory studies on novel azide metal complexes. Future Med. Chem. **16**(11), 1109–1125 (2024)

31. Y. Zhao, D.G. Truhlar, Applications and validations of the Minnesota density functionals. Chem. Phys. Lett. **502**, 1–13 (2011)
32. P. Verma, Z. Varga, J.E.M.N. Klein, C.J. Cramer, LJr. Que, D.G. Truhlar, Assessment of electronic structure methods for the determination of the ground spin states of Fe(II), Fe(III) and Fe(IV) complexes. Phys. Chem. Chem. Phys. **19**, 13049–13069 (2017)
33. S. Altürk, D. Avcı, Ö. Tamer, Y. Atalay, Comparison of different hybrid DFT methods on structural, spectroscopic, electronic and NLO parameters for a potential NLO material. Comput. Theor. Chem. **1100**, 34–45 (2017). https://doi.org/10.1016/j.comptc.2016.12.007
34. N.E. Schultz, Y. Zhao, D.G. Truhlar, Density functionals for inorganometallic and organometallic chemistry. J. Phys. Chem. A **109**(49), 11127–11143 (2005). https://doi.org/10.1021/jp053922 3
35. Y. Zhao, D.G. Truhlar, The M06 suite of density functionals for main group thermochemistry, thermochemical kinetics, noncovalent interactions, excited states, and transition elements: two new functionals and systematic testing of four M06-class functionals and 12 other functionals. Theor. Chem. Acc. **120**(1–3), 215–241 (2008). https://doi.org/10.1007/s00214-007-0310-x
36. G.M. Sheldrick, SHELXT – integrated space-group and crystal-structure determination. Acta Cryst. **A71**, 3–8 (2015)
37. C.F. Macrae, P.R. Edgington, P. McCabe, E. Pidcock, G.P. Shields, R. Taylor, M. Towler, J. van de Streek, Mercury visualization and analysis of crystal structures. J. Appl. Crystallogr. **39**, 453–457 (2006)
38. A.L. Spek, Structure validation in chemical crystallography. Acta Cryst. **D65**, 148–155 (2009)
39. H. Sun, W.N. Ding, X.T. Song, D. Wang, M.Z. Chen, K.L. Wang, Y.Z. Zhang, P. Yuan, Y. Ma, R.L. Wang, R.H. Dodd, Y.M. Zhang, K. Lu, P. Yu, Synthesis of 6-hydroxyaurone analogues and evaluation of their α-glucosidase inhibitory and glucose consumption-promoting activity: development of highly active 5, 6-disubstituted derivatives. Bioorg. Med. Chem. Lett. **27**, 3226–3230 (2017)
40. Gaussian 16, Revision C.01, M. J. Frisch, G. W. Trucks, H. B. Schlegel, G. E. Scuseria, M. A. Robb, J. R. Cheeseman, G. Scalmani, V. Barone, G. A. Petersson, H. Nakatsuji, X. Li, M. Caricato, A. V. Marenich, J. Bloino, B. G. Janesko, R. Gomperts, B. Mennucci, H. P. Hratchian, J. V. Ortiz, A. F. Izmaylov, J. L. Sonnenberg, D. Williams-Young, F. Ding, F. Lipparini, F. Egidi, J. Goings, B. Peng, A. Petrone, T. Henderson, D. Ranasinghe, V. G. Zakrzewski, J. Gao, N. Rega, G. Zheng, W. Liang, M. Hada, M. Ehara, K. Toyota, R. Fukuda, J. Hasegawa, M. Ishida, T. Nakajima, Y. Honda, O. Kitao, H. Nakai, T. Vreven, K. Throssell, J. A. Montgomery, Jr., J. E. Peralta, F. Ogliaro, M. J. Bearpark, J. J. Heyd, E. N. Brothers, K. N. Kudin, V. N. Staroverov, T. A. Keith, R. Kobayashi, J. Normand, K. Raghavachari, A. P. Rendell, J. C. Burant, S. S. Iyengar, J. Tomasi, M. Cossi, J. M. Millam, M. Klene, C. Adamo, R. Cammi, J. W. Ochterski, R. L. Martin, K. Morokuma, O. Farkas, J. B. Foresman, and D. J. Fox, Gaussian, Inc., Wallingford CT, 2016.
41. GaussView, Version 6.1, R. Dennington, T.A. Keith, J.M. Millam, Semichem Inc., Shawnee Mission, KS, 2016.
42. T. Yanai, D.P. Tew, N.C. Handy, A new hybrid Exchange-correlation functional using the Coulomb-attenuating method (CAM-B3LYP). Chem. Phys. Lett. **393**, 51–57 (2004)
43. A.D. Boese, N.C. Handy, A new parametrization of exchange-correlation generalized gradient approximation functionals. J. Chem. Phys. **114**, 5497–5503 (2001)
44. F.A. Hamprecht, A. Cohen, D.J. Tozer, N.C. Handy, Development and assessment of new exchange-correlation functionals. J. Chem. Phys. **109**(15), 6264–6271 (1998). https://doi.org/10.1063/1.477267
45. A.D. Boese, N.L. Doltsinis, N.C. Handy, M. Sprik, New generalized gradient approximation functionals. J. Chem. Phys. **112**(4), 1670–1678 (2000). https://doi.org/10.1063/1.480732
46. Y. Zhao, D.G. Truhlar, A new local density functional for main-group thermochemistry, transition metal bonding, thermochemical kinetics, and noncovalent interactions. J. Chem. Phys. **125**(19), 194101 (2006). https://doi.org/10.1063/1.2370993
47. J.M. Tao, J.P. Perdew, V.N. Staroverov, G.E. Scuseria, Climbing the density functional ladder: nonempirical meta-generalized gradient approximation designed for molecules and solids. Phys. Rev. Lett. **91**(14), 146401 (2003). https://doi.org/10.1103/PhysRevLett.91.146401
48. P.J. Hay, W.R. Wadt, Ab initio effective core potentials for molecular calculations. Potentials for the transition metal atoms Sc to Hg. J. Chem. Phys. **82**, 270–283 (1985)
49. M. H. Jamroz, Vibrational energy distribution analysis VEDA 4, in, Warsaw Poland, 2004.
50. M.H. Jamróz, Vibrational energy distribution analysis (VEDA): scopes and limitations. Spectrochim. Acta A Mol. Biomol. Spectrosc. **114**, 220–230 (2013). https://doi.org/10.1016/j.saa.2013.05.096
51. E.D. Glendening, A.E. Reed, J.E. Carpenter, F. Weinhold, NBO Version3.1, TCI, University of Wisconsin, Madison, 1998.
52. S. Miertus, E. Scrocco, J. Tomasi, Electrostatic interaction of a solute with a continuum. A direct utilizaion of AB initiomolecular potentials for the prevision of solvent effects. J. Chem. Phys. **55**, 117–129 (1981)
53. S.I. Gorelsky, SWizard Program, Revision 4.5, University of Ottawa, Ottawa, Canada, 2010, http://www.sg.chem.net/.
54. L. Skripnikov, Chemissian: software to analyze spectra, build density maps and molecular orbitals, Version 4 (43) (2016).
55. G.M. Morris, R. Huey, W. Lindstrom, M.F. Sanner, R.K. Belew, D.S. Goodsell, A.J. Olson, Autodock4 and AutoDockTools4: automated docking with selective receptor flexibility. J. Comput. Chem. **30**, 2785–2791 (2009)
56. M.F. Sanner, Python: a programming language for software integration and development. J. Mol. Graph. Model. **17**, 57–61 (1999)
57. G.M. Morris, D.S. Goodsell, R.S. Halliday, R. Huey, W.E. Hart, R.K. Belew, A.J. Olson, Automated docking using a lamarckian genetic algorithm and and empirical binding free energy function. J. Comput. Chem. **19**(14), 1639–1662 (1998)
58. Ö. Özge, D. Avcı, F. Sönmez, Ö. Tamer, N. Dege, A. Başoğlu, Y. Atalay, B. Zengin Kurt, Synthesis, DFT calculations, α-glucosidase inhibitor activity, and docking studies on Schiff base metal complexes containing isothiocyanate. Appl. Organomet. Chem. **37**, e7084 (2023)
59. D. Systèmes, Dassault Systèmes Biovia: San Diego, CA, USA (2016)
60. A.E. Reed, F. Weinhold, Natural bond orbital analysis of near-Hartree–Fock water dimer. J. Chem. Phys. **78**(6), 4066–4073 (1983). https://doi.org/10.1063/1.445134
61. J.P. Foster, F. Weinhold, Natural hybrid orbitals. J. Am. Chem. Soc. **102**, 7211–7218 (1980)
62. Y. Tantirungrotechai, K. Phanasant, S. Roddecha, P. Surawatanawong, V. Sutthikhum, J. Limtrakul, Scaling factors for vibrational frequencies and zero-point vibrational energies of some recently developed exchangecorrelation functionals. J.

Mol. Struct. THEOCHEM **760**(1–3), 189–192 (2006). https://doi.org/10.1016/j.theochem.2005.12.007
63. J.P. Merrick, D. Moran, L. Radom, An evaluation of harmonic vibrational frequency scale factors. J. Phys. Chem. A **111**, 11683–11700 (2007)
64. D. Avcı, Y. Atalay, Theoretical analysis of vibrational spectra and scaling-factor of 2-aryl-1,3,4-oxadiazole derivatives. Int. J. Quantum Chem. **109**(2), 328–341 (2009)
65. M. Biczysko, P. Panek, V. Barone, Toward spectroscopic studies of biologically relevant systems: vibrational spectrum of adenine as a test case for performances of long-range/dispersion corrected density functionals. Chem. Phys. Lett. **475**, 105–110 (2009)
66. M. Malik, D. Michalska, Assessment of new DFT methods for predicting vibrational spectra and structure of cisplatin: which density functional should we choose for studying platinum(II) complexes? Spectrochim. Acta A **125**, 431–439 (2014)
67. I.M. Alecu, J. Zheng, Y. Zhao, D.G. Truhlar, Computational thermochemistry: scale factor databases and scale factors for vibrational frequencies obtained from electronic model chemistries. J. Chem. Theory Comput. **6**, 2872–2887 (2010)
68. D. Avcı, Y. Saeedi, A. Başoğlu, N. Dege, S. Altürk, Ö. Tamer, Y. Atalay, Novel Mn(II) and Zn(II) complexes of 6-bromopicolinic acid as a potential optical material: synthesis, spectral characterizations, linear, and nonlinear optical properties and density functional theory calculations. Appl. Organomet. Chem. **35**, e6125 (2021)
69. J. Tauc, A. Menth, States in the gap. J. Non Cryst. Solids **8**, 569–585 (1972)
70. A. Adachi, A. Kudo, T. Sakata, The optical and photoelectrochemical properties of electrodeposited CdS and SnS thin films. Bull. Chem. Soc. Jpn **68**, 3283–3288 (1995)
71. J. Šponer, P. Hobza, DNA base amino groups and their role in molecular interactions: ab initio and preliminary density functional theory calculations. Int. J. Quant. Chem. **57**, 959–970 (1996)
72. S.R. Gadre, I.H. Shrivastava, Shapes and sizes of molecular anions via topographical analysis of electrostatic potential. J. Chem. Phys. **94**, 4384–4390 (1991)
73. M. Sheik-Bahae, A.A. Said, E.W. Van Stryland, High-sensitivity, single-beam n_2 measurements. Opt. Lett. **14**, 955–957 (1989)
74. M. Sheik-Bahae, A.A. Said, T.H. Wei, D.J. Hagan, E.W. Van Stryland, Sensitive measurement of optical nonlinearities using a single beam. IEEE J. Quantum Electron. **26**(4), 760–768 (1990)
75. M.G. Kuzyk, C.W. Dirk, *Characterization techniques and tabulations for organic nonlinear optical materials* (Marcel Dekker, Inc., New York, 1998), p.655
76. D. Wang, S. Wang, J. Wang, C. Shen, W. Li, P. Huang, H. Liu, R.I. Boughton, Research on nonlinear absorption effect in KDP and 70%-DKDP crystals. Crystals **7**, 188 (2017)
77. R.A. Ganeev, I.A. Kulagin, A.I. Ryasnyansky, R.I. Tugushev, T. Usmanov, Characterization of nonlinear optical parameters of KDP, $LiNbO_3$ and BBO crystals. Opt. Commun. **229**(1–6), 403–412 (2004). https://doi.org/10.1016/j.optcom.2003.10.046
78. D. Wang, T. Li, S. Wang, J. Wang, Z. Wang, X. Xua, F. Zhang, Study on nonlinear refractive properties of KDP and DKDP crystals. RSC Adv. **6**, 14490–14495 (2016)
79. P. Justin, M. Tamilelakkiya, A. Mythili, P. Velusamy, K. Anitha, Investigation on the structure, optical, thermal, Z-scan, and DFT characteristics of nitrobenzimidazolium phthalate monohydrate single crystal. J. Mater. Sci. Mater. Electron. **36**, 770 (2025)
80. V. Periyasamy, R.B. Ramraj, I. Hasan, P. Subramanian, I. Kim, S. Paramasivam, Characterization of single-crystal phenothiazine synthesized using the vertical Bridgman method. Z. Phys. Chem. **238**(11), 2121–2134 (2024). https://doi.org/10.1515/zpch-2023-0491
81. S. Singaravel, V. Periyasamy, I. Kim, I. Hasan, S. Paramasivam, Single crystal of barium bis paranitrophenolate *para*-nitrophenol tetrahydrate for NLO applications: crystal growth and DFT analysis. Z. Phys. Chem. **238**(11), 2101–2119 (2024)
82. S.P. Prabhakaran, R.R. Babu, P. Velusamy, K. Ramamurthi, Studies on the growth, structural, optical, mechanical properties of 8-hydroxyquinoline single crystal by vertical Bridgman technique. Mater. Res. Bull. **46**(11), 1781–1785 (2011). https://doi.org/10.1016/j.materresbull.2011.08.001
83. M.M. El-Nahass, A.A.M. Farag, Structural, optical and dispersion characteristics of nanocrystalline GaN films prepared by MOVPE. Optics Laser Technol. **44**(2), 497–503 (2012). https://doi.org/10.1016/j.optlastec.2011.08.021
84. M.D. Bharathi, G. Ahila, J. Mohana, G. Chakkaravarthi, G. Anbalagan, Synthesis, crystal structure, growth, optical and third order nonlinear optical studies of 8HQ2C5N single crystal-an efficient third-order nonlinear optical material. Mater. Chem. Phys. **192**, 215–227 (2017). https://doi.org/10.1016/j.matchemphys.2017.01.087
85. L.T. Cheng, W. Tam, S.H. Stevenson, G.R. Meredith, G. Rikken, S.R. Marder, Experimental investigations of organic molecular nonlinear optical polarizabilities. 1. Methods and results on benzene and stilbene derivatives. J. Phys. Chem. **95**, 10631–10643 (1991)
86. I. Ledoux, J. Zyss, Influence of the molecular environment in solution measurements of the second-order optical susceptibility for urea and derivatives. Chem. Phys. **73**, 203–213 (1982)
87. C. Adant, M. Dupuis, J. Bredas, Ab initio study of the nonlinear optical properties of urea: electron correlation and dispersion effects. Int. J. Quantum Chem. **56**, 497–507 (1995)
88. M. Şimşek, D. Avcı, F. Sönmez, A. Başoğlu, Ö. Tamer, Y. Atalay, Unveiling the NLO potential of new Zn (II) complex of 6-methylpyridine-2-carboxaldehyde: experimental/DFT study on spectral, static, and frequency-dependent linear/nonlinear optical parameters. Appl. Organomet. Chem. **39**, e7798 (2025)
89. D. Avcı, Ö. Özge, F. Sönmez, A. Başoğlu, Ö. Tamer, Y. Atalay, Novel Schiff base-azide metal complexes: synthesis, spectral, nonlinear optics, and DFT studies. Mater. Sci. Semicond. Process. **179**, 108523 (2024)
90. S. Bullo, R. Jawaria, I. Faiz, I. Shafiq, M. Khalid, M.A. Asghar, R. Baby, R. Orfali, S. Perveen, Efficient synthesis, spectroscopic characterization, and nonlinear optical properties of novel salicylaldehyde-based thiosemicarbazones: experimental and theoretical studies. ACS Omega **8**, 13982–13992 (2023)
91. X.-y Yang, W.-D. Xiang, Third-order optical nonlinearity of CdS nanocrystals embedded in sodium borosilicate glass studied by the Z-scan technique. J. Mater. Res. **25**(3), 491–499 (2010)
92. A. Tahmasbi, A. Jafari, A. Nikoo, Synthesis, characterization, and nonlinear optical properties of copper (II) ligand Schiff base complexes derived from 3-nitrobenzohydrazide and benzyl. Sci. Rep. **13**, 10988 (2023)
93. S. Kamaal, M. Mehkoom, A. Ali, S.M. Afzal, M.J. Alam, S. Ahmad, M. Ahmad, Potential third-order nonlinear optical response facilitated by intramolecular charge transfer in a simple Schiff base molecule: experimental and theoretical exploration. ACS Omega **6**, 6185–6194 (2021)

94. K. Boopathi, S.M. Babu, R. Jagan, P. Ramasamy, Synthesis, crystal structure and growth of a new inorganic- organic hybrid compound for nonlinear optical applications: aquadiiodo (3-aminopropanoic acid) cadmium (II). J. Phys. Chem. Solids **111**, 419–430 (2017). https://doi.org/10.1016/j.jpcs.2017.08.038
95. H. Ali, A. Anjum, D. Goswami, Investigating the third-order nonlinear optical properties of a Schiff base (DBAP) and its Co/Cu metal complex using Z-scan and DFT methodology. J. Mol. Struct. **1307**, 138039 (2024)
96. M. Shkir, S. Muhammad, S. AlFaify, A. Irfan, P.S. Patil, M. Arora, H. Algarni, Z. Jingping, An investigation on the key features of a D–π–a type novel chalcone derivative for optoelectronic applications. RSC Adv. **5**, 87320–87332 (2015)
97. M. Shkir, S. AlFaify, M. Arora, V. Ganesh, H. Abbas, I.S. Yahia, A first principles study of key electronic, optical, second and third order nonlinear optical properties of 3-(4-chlorophenyl)-1-(pyridin-3-yl)prop-2-en-1-one: a novel D-π-A type chalcone derivative. J. Comput. Electron. **17**, 9–20 (2018)
98. B.C. Raju, A.K. Tiwari, J.A. Kumar, A.Z. Ali, S.B. Agawane, G. Saidachary, K. Madhusudana, α-Glucosidase inhibitory antihyperglycemic activity of substituted chromenone derivatives. Bioorg. Med. Chem. **18**(1), 358–365 (2010). https://doi.org/10.1016/j.bmc.2009.10.047
99. M. Khan, G. Ahad, A. Alam, S. Ullah, A. Khan, K.U. Salar, A. Wadood, A. Ajmal, K.M. Khan, S. Perveen, J. Uddin, A. Al-Harras, Synthesis of new bis (dimethylamino)benzophenone hydrazone for diabetic management: *in-vitro* and *in-silico* approach. Heliyon **10**, e23323 (2024)
100. M.M. Hermans, M.A. Kroos, J. van Beeumen, B.A. Oostra, A.J. Reuser, Human lysosomal alpha-glucosidase. Characterization of the catalytic site. J. Biol. Chem. **266**(21), 13507–13512 (1991)
101. C.S. Rye, S.G. Withers, Glycosidase mechanisms. Curr. Opin. Chem. Biol. **4**(5), 573–580 (2000)
102. Q. Dong, N. Hu, H. Yue, H. Wang, Inhibitory activity and mechanism investigation of hypericin as a novel α-glucosidase inhibitor. Molecules **26**(15), 4566 (2021)
103. J. Zheng, L. Ma, Silver(I) complexes of 2,4-dihydroxybenzaldehyde–amino acid Schiff bases-novel noncompetitive α-glucosidase inhibitors. Bioorg. Med. Chem. Lett. **25**, 2156–2161 (2015)
104. J.W. Zheng, L. Ma, Assessment of silver(I) complexes of salicylaldehyde derivatives histidine Schiff base as novel α-glucosidase inhibitors. Chin. Chem. Lett. **27**(2), 283–286 (2016). https://doi.org/10.1016/j.cclet.2015.11.015
105. Y. Wang, L. Ma, Z. Li, Z. Du, Z. Liu, J. Qin, X. Wang, Z. Huang, L. Gu, A.S.C. Chen, Synergetic inhibition of metal ions and genistein on α-glucosidase. FEBS Lett. **576**(1–2), 46–50 (2004). https://doi.org/10.1016/j.febslet.2004.08.059
106. D. Avcı, S. Altürk, F. Sönmez, Ö. Tamer, A. Başoğlu, Y. Atalay, B. Zengin Kurt, D. Öztürk, N. Dege, A new dinuclear copper (II) complex of 2, 5–Furandicarboxyclic acid with 4 (5)-Methylimidazole as a high potential α-glucosidase inhibitor: synthesis, crystal structure, cytotoxicity study, and TD/DFT calculations. Appl. Organomet. Chem. **33**(3), e4725 (2019)
107. S.V. Saravanaselvam, X. Arulanantham, M. Tamilelakkiya, R. Sakthivadivel, S. Ponnusamy, P. Pandi, P. Velusamy, S.E. Muthu, K.A. Kumar, Synthesis and characterization of novel Schiff base ligand and their Cu (II), Zn (II), Co (II), and Ni (II) complexes: DNA binding, antimicrobial activity and docking studies]. Considering the moderate inhibition value of the Cd(II) complex in this study and the above results, the cytotoxicity study was not taken into consideration. J. Mol. Struct. **1325**, 141000 (2025)